

POLITECNICO DI TORINO

Master of science program in
MECHANICAL ENGINEERING



Master's degree thesis

The development and calibration of turbulence modelling for turbomachinery applications

Supervisor:

Prof. Roberto Marsilio

Prof. Davide Lengani

Prof. Dario Barsi

Candidate:

Yueliang Zhang

Abstract

With the development of society and economy, higher requirements are put forward for turbomachinery, including economy, stability, and low emissions. High-performance computers have enabled numerical simulation to play an increasingly important role in improving turbomachinery performance. Although DNS and LES can simulate the actual situation more accurately, limited by computer capabilities and economic factors, the work in this paper will focus on comparing the differences between RANS/URANS and DNS, and modify the boundary conditions in various ways to improve the simulation accuracy.

After completing the grid independence verification, the pressure coefficient, skin friction coefficient, total pressure and loss of multiple turbulence models including k-omega model were compared to find a better choice. Turbulence intensity values of k-omega model with transition options and Transition SST model have been modified in order to identify the best matching between RANS and DNS with different turbulence intensity in terms of turbulence behavior on blade profile.

In order to further simulate the complex flow of the multi-stage compressor and the losses caused by the flow, the boundary conditions were compiled using UDF. It is worth noting that the inlet boundary conditions were obtained in an iterative way from outlet conditions provided by simulations. Finally, by comparing the results of DNS and URANS under various operating conditions, losses from URANS are more in accordance with DNS with respect to RANS.

Key words: RANS/URANS; DNS; Turbulence intensity; Loss

Table of contents

Abstract.....	III
List of figures.....	VI
List of tables.....	IX
Nomenclature.....	X
1 Introduction.....	1
1.1 Motivation.....	1
1.2 Outline.....	3
2 Literature Review.....	4
2.1 Turbulence model.....	4
2.2 Turbomachinery	5
2.3 Concluding remarks	7
3 Computational Methods.....	8
3.1 Numerical simulation model.....	8
3.2 Meshing.....	10
3.3 Numerical set up	12
3.3.1 Continuity and Momentum Equations	12
3.3.2 Turbulence.....	13
3.3.3 Grid independence verification.....	14
3.3.4 Turbulence Model Comparison.....	18
4 Result and discussion.....	21
4.1 Steady case.....	21
4.1.1 Compared with DNS with Tu equals to 6%.....	21
4.1.2 Compared with DNS with Tu equals to 4%.....	29
4.1.3 Defining boundary conditions using UDF	37
4.1.4 Conclusions.....	41
4.2 Unsteady case.....	43
4.2.1 URANS comparisons.....	43
4.2.2 Conclusions.....	58

4.3 Conclusions.....	58
5 Conclusions and Recommendations for Future Work	60
Acknowledge	62
Bibliography	64

List of figures

1.1 Turbulence modelling hierarchy. [2]	2
3.1 Compressor Cascade [30]	9
3.2 2D single channel cascade	10
3.3 Cascade model created by SolidWorks	11
3.4 Example mesh and block structure	11
3.5 Grids with different numbers of nodes	15
3.6 Block division of DNS and drawing line of turbulence intensity	16
3.7 Grid independence verification comparison	17
3.8 Turbulence Model Comparison	18
4.1 Comparison of turbulence intensity between DNS (Tu=6%) and k-omega model with transition options	21
4.2 Comparison of velocity and boundary layer of k-omega model with transition options under different turbulence intensities (higher turbulence intensity)	22
4.3 Comparison of static pressure of k-omega model with transition options under different turbulence intensities (higher turbulence intensity)	23
4.4 Comparison of turbulence intensity of k-omega model with transition options under different turbulence intensities (higher turbulence intensity)	23
4.5 Comparison of turbulence intensity between DNS (Tu=6%) and Transition SST model	26
4.6 Comparison of velocity and boundary layer of Transition SST model under different turbulence intensities (higher turbulence intensity)	27
4.7 Comparison of static pressure of Transition SST model under different turbulence intensities (higher turbulence intensity)	27
4.8 Comparison of turbulence intensity of Transition SST model under different turbulence intensities (higher turbulence intensity)	28
4.9 Comparison of turbulence intensity between DNS (Tu=4%) and k-omega model with transition options	30

4.10 Comparison of velocity and boundary layer of k-omega model with transition options under different turbulence intensities (lower turbulence intensity).....	31
4.11 Comparison of static pressure of k-omega model with transition options under different turbulence intensities (lower turbulence intensity)	31
4.12 Comparison of turbulence intensity of k-omega model with transition options under different turbulence intensities (lower turbulence intensity)	32
4.13 Comparison of turbulence intensity between DNS (Tu=4%) and Transition SST model	34
4.14 Comparison of velocity and boundary layer of Transition SST model under different turbulence intensities (lower turbulence intensity)	35
4.15 Comparison of static pressure of Transition SST model under different turbulence intensities (lower turbulence intensity)	35
4.16 Comparison of turbulence intensity of Transition SST model under different turbulence intensities (lower turbulence intensity)	36
4.17 Schematic of the computational domain and wake recycling procedure	37
4.18 Inlet total pressure for steady case	37
4.19 Outlet velocity angle	38
4.20 Y-Component of Flow Direction	38
4.21 Comparison of parameters before and after UDF compilation boundary conditions.....	39
4.22 Velocity contours before and after UDF compilation of boundary conditions ...	40
4.23 Pressure contours before and after UDF compilation of boundary conditions...	40
4.24 Turbulence intensity cloud map before and after UDF compilation of boundary conditions	41
4.25 Velocity contour with UDF compiles inlet pressure	43
4.26 Comparison between RANS and average velocity contour with UDF compiles inlet pressure	44
4.27 Pressure contour with UDF compiles inlet pressure	44

4.28 Comparison between RANS and average pressure contour with UDF compiles inlet pressure	45
4.29 Velocity contour with UDF compiles inlet pressure and angle	46
4.30 Comparison between RANS and average velocity contour with UDF compiles inlet pressure and angle	47
4.31 Pressure contour with UDF compiles inlet pressure and angle	47
4.32 Comparison between RANS and average pressure contour with UDF compiles inlet pressure and angle	48
4.33 Skin friction coefficient with pressure inlet (URANS)	49
4.34 X-Velocity for Velocity Inlet	49
4.35 Y-Velocity for Velocity Inlet	50
4.36 Skin friction coefficient with velocity inlet (URANS)	50
4.37 Skin friction coefficient for DNS	51
4.38 Comparison of specific dissipation rate using turbulence intensity inlet and turbulent kinetic energy inlet	52
4.39 Average turbulence intensity at the inlet and at the sampling plane of the domain for the NACA65 testcase [27]	52
4.40 Skin friction coefficient comparison (Turbulence intensity is 10% in wake region)	53
4.41 Skin friction coefficient comparison (Turbulence intensity is 5% except in wake region)	53
4.42 Skin friction coefficient comparison (Turbulence intensity is 3% except in wake region)	53
4.43 Boundary layer momentum thickness (URANS)	55
4.44 Boundary layer displacement thickness (URANS)	55
4.45: Boundary layer momentum thickness (DNS)	56
4.46 Boundary layer displacement thickness (DNS)	56

List of tables

3.1 Profile Coordinates [30]	9
3.2 Grid parameters	15
4.1 Comparison of parameters under different inlet turbulence intensity between DNS(Tu=6%) and k-omega model with transition options	22
4.2 Comparison of parameters under different inlet turbulence intensity between DNS(Tu=6%) and Transition SST model	26
4.3 Comparison of parameters under different inlet turbulence intensity between DNS(Tu=4%) and k-omega model with transition options	30
4.4 Comparison of parameters under different inlet turbulence intensity between DNS(Tu=4%) and Transition SST model	34
4.5 Pressure loss for URANS	57
4.6 Pressure loss for DNS	57

Nomenclature

Roman Symbols

C_{ax}	Axial chord
C_f	Skin friction coefficient
C_p	Pressure coefficient
C_{pb}	Base pressure coefficient
CFD	Computational Fluid Dynamics
DNS	Direct Numerical Simulation
I	Unit tensor
$k\omega$	k-omega model
$k\omega T$	k-omega model with transition options
l	Blade chord
LES	Large Eddy Simulation
P	Static pressure
P^*	Stagnation pressure
RANS	Reynolds-Averaged Navier-Stokes
SA	Spalart-Allmaras model
t	Blade spacing
t_e	Trailing edge thickness
Tk	Transition k-k-kl-omega model
TS	Transition SST model
URANS	Unsteady Reynolds-Averaged Navier-Stokes
\vec{v}	Velocity vector
V	Velocity
w	Throat width

Greek Symbols

β	Flow angle
---------	------------

β_s	Stagger angle
δ^*	Boundary layer displacement thickness
ξ	Pressure loss
θ	Boundary layer momentum thickness
μ	Molecular viscosity
τ	Shear stress
$\bar{\tau}$	Stress tensor
ρ	Density
ϕ	Total pressure loss coefficient

Subscripts

1	Inlet condition for the cascade
2	Outlet condition for the cascade
ref	Reference
te	Just before the trailing edge

1 Introduction

1.1 Motivation

How to improve the efficiency of turbomachinery is a hot topic of research in the world today, and the complex flow inside the turbomachinery, also the complex structure of the turbomachinery, make the research difficult.[1] The development of turbomachinery requires high research and development costs. For example, the development of gas turbines can easily exceed 500 million pounds. In addition, although experimental research can find problems more accurately, the experimental cost is high and experimental period is very long. So pure experimentation is not the most effective research method. Coupled with the rapid development of computing, all this has spawned the rapid development of Computational Fluid Dynamics (CFD) and created a lot of economic benefits. Numerical simulations have been developed over a long period, where trends in turbomachinery turbulence treatments was introduced by P.G. Tucker. [2] As noted by Denton [3] and Menter et al. [4], how to predict the development of turbulence is an important means to design and test the performance of turbomachinery.

Turbomachinery is used in a wide range of applications, such as the aviation industry, power generation and navigation. In the society, in order to achieve ambitious emissions and efficiency goals, turbomachinery design is bound to undergo earth-shaking changes. The EU Flightpath 2050 report points out that by 2050, NO_x will be reduced by 90% and CO₂ by 75% compared to 2000.[5] James et al. summarized the challenges and future of numerical simulation of turbomachinery.[6] Of course Direct Numerical Simulation (DNS) [7][8][9] is the most effective research method, other than Large Eddy Simulation (LES),[10][11][12] but these research methods require high-

performance computers. At the current stage, it is difficult to achieve large-scale promotion and application. Reynolds-Averaged Navier-Stokes/ Unsteady Reynolds-Averaged Navier-Stokes (RANS/URANS) [13][14] is still the most important research method. It is undeniable that compared with DNS, RANS/URANS is difficult to capture some minor changes in the simulation process. How to minimize this error through modification is an effective way to improve calibration.

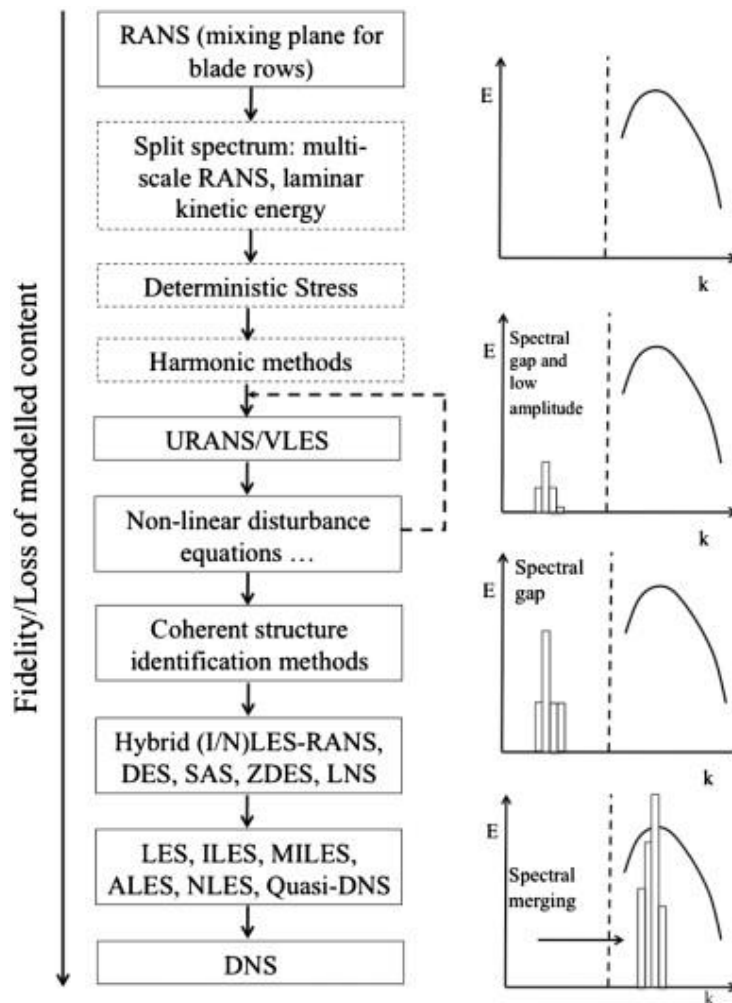


Figure 1.1: Turbulence modelling hierarchy. [2]

Currently, there are many high-fidelity computational fluid dynamics (CFD) simulations, such as DNS and LES, [15] [16] [17] but these research methods require large-scale computer clusters. In order to save computational resources and improve

the efficiency of numerical simulation, this work will compare the numerical simulation results of RANS/URANS and DNS in some aspects, and minimize the difference between RANS/URANS and DNS by modifying the calculation model, inlet and outlet conditions through various modes to improve the fidelity of the numerical simulation.

1.2 Outline

The thesis begins with a literature review in Chapter 2, which includes the current state of research on turbulence model and numerical simulations of turbines and compressors. The third chapter introduces the model creation, turbulence model and various settings of numerical simulation in detail. The fourth chapter comprehensively compares the differences between RANS and DNS, URANS and DNS, under different working conditions. The last chapter draws conclusions and looks forward to the work that can be continued in the future.

2 Literature Review

In the past 30 years, CFD has ushered in a revolutionary development. Although CFD has developed very rapidly, there are still many problems that need to be solved.[18] Continuous efforts and innovative methods are needed to solve the computational inaccuracy problem of CFD.[19] CFD began to gain attention in the 1970s and has since led to major changes in the design of commercial aircraft. [20] After entering the 1980s, the required solution equation became the Navier-Stokes equation. Since then, the development of CFD has become relatively mature and has become an important means of analyzing problems in the scientific community. The reason why CFD has grown so rapidly is inseparable from the two motivations of providing important new technologies and capabilities and economics.[21] In the aerospace field, the use of compressible Navier-Stokes equations to simulate actual flow only began to appear in 1985.

2.1 Turbulence model

In 2022, Yi Yang et al. of Beihang University used the RANS/LES hybrid method to study the tip instability and turbulence characteristics of transonic turbine cascades. Through the identification and extraction of vortices, two unstable features of vortex rupture and vortex drift were observed with a relatively small number of meshes. Compared with RANS, which uses RANS to study the boundary layer, LES studies the hybrid method far away from the boundary layer to capture these unstable properties more easily.[22]

In 2020, Marco Tiberga et al. of Delft University of Technology investigated the use of a high-order discontinuous Galerkin solver to solve incompressible RANS equations. By extending the laminar flow solver and coupling it into the k-epsilon model, the

pressure correction method is finally used to solve the incompressible RANS equation. Compared with the traditional k-epsilon model, the optimized turbulence model is more similar to the DNS/LES results.[23]

S. Kubacki et al. (2016) of Warsaw University of Technology discussed the application of algebraic intermittent models to predict bypass and separation induced boundary layer transitions. The transition model is combined with the k- ω turbulence model. The transition model uses only local variables and is adjusted for turbomachinery flow. For RANS, the model can more accurately simulate transitions caused by bypass and separation, and for URANS, the model can more accurately simulate transitions caused by wake.[24]

In 2009 Keith Walters of Mississippi State University studied Transition-Sensitive of RANS model. Through research, it is found that when there are fluctuations in the external environment, the transition caused by separation, the boundary layer needs to withstand a larger reverse pressure gradient. In addition, a more common type of bypass transition involves the triggering of streaks by external fluctuations. Due to their convective phenomena downstream, the streaks become unstable and eventually become turbulent points.[13]

2.2 Turbomachinery

Non-equilibrium boundary layer modeling of three compressor blade geometries using RANS and other high-fidelity simulations was researched by Robert Spencer et al. (2021) It is found that for low Reynolds number conditions, Boussinesq assumption tends to lead to an under prediction in peak turbulence production and an over prediction of skin-friction. Capturing the correct unbalanced behavior requires modification of the standard k - ω SST model. It was found that the model constant β_1 needs to be reduced to match the non-equilibrium behavior of the suction side. Non-

equilibrium effects can correct up to a 40% increase in trailing edge momentum thickness. [25]

In 2020, Pawel J. Przytarski et al. of the University of Cambridge used the outlet parameters of the single-stage blade as the inlet condition, effectively completed the repeated multi-channel numerical simulation, and found that a smaller axial clearance would increase the dissipation by 5.5% to 9.5%. And in 2018, the effect of resolution on viscous dissipation was investigated by simulating Taylor-Green vortex canonical flow, and by capturing instability mechanisms upstream of the transition, and subsequent turbulence studies on dissipation. The interaction of free-stream turbulence at the leading-edge and development of streaks in the laminar region of the boundary layer was found to be an important factor affecting dissipation.[26][27]

T. A. Zaki · J. G of Imperial College London in 2009, based on the setup of the experiments performed by Hilgenfeld and Pfitzner, used direct numerical simulations to study the migrating tail. The effect of flow on the boundary layer. The study found that the boundary layer along the suction side of the blade separates and rolls up. A further transition to turbulent flow was found to occur inside the roll. The boundary layer flow along the pressure side is not separated but undergoes a bypass transition.[28]

In 2004, Lothar Hilgenfeld of Universitaet der Bundeswehr Muenchen et al studied the influence of wake effect on compressor cascade. For highly loaded linear compressor cascades, the wake will cause a significant reduction in the time-averaged momentum thickness, along with the presence and amplification of velocity oscillations in the boundary layer, illustrating the possibility of reduction at any time.[29]

2.3 Concluding remarks

This chapter mainly introduces some research progress related to this paper in the field of turbulence model and turbomachinery, although DNS and LES have carried out many high-fidelity numerical simulation studies, and even a mixture of RANS and LES has been carried out. However, limited by the development of computers and the complexity of research, RANS and URANS are still the main numerical simulation methods.

This chapter shows that in order to adapt to numerical simulations with higher requirements, traditional turbulence models need to be further optimized to capture more changes to achieve accurate simulations, such as the study of boundary layers, wakes, and turbulence intensity studies. The research method fully compares the numerical differences between RANS/URANS and DNS in various aspects, so as to further pave the way for subsequent optimization work.

3 Computational Methods

ANASYS is used for studies discussed in this thesis. The accuracy of ANSYS can be very well guaranteed in the process of numerical simulation of low-velocity blades. This chapter introduces all the preprocessing and the theoretical part involved.

3.1 Numerical simulation model

NACA 65 is used as research object in this thesis and it includes two sides including pressure side and suction side with 31 points.

Suction side		Pressure side	
x/l	y/l	x/l	y/l
0.0000000	0.0000000	0.0000000	0.0000000
-.0002600	0.0012215	0.0010000	-.0012223
0.0010000	0.0036653	0.0027400	-.0017785
0.0067114	0.0082726	0.0067114	-.0011683
0.0134228	0.0130225	0.0134228	-.0001393
0.0201342	0.0172630	0.0201342	0.0013155
0.0335570	0.0249829	0.0335570	0.0047198
0.0402685	0.0285939	0.0402685	0.0065403
0.0536913	0.0354450	0.0536913	0.0102781
0.1006709	0.0566955	0.1006709	0.0232978
0.0610731	0.0794272	0.1610731	0.0384398
0.2214754	0.0978480	0.2214754	0.0512036
0.2818777	0.1122796	0.2953004	0.0634820
0.3489913	0.1238375	0.3624141	0.0715853
0.4026822	0.1297438	0.4161050	0.0760471
0.4697959	0.1330142	0.4832186	0.0791789

0.5234868	0.1323615	0.5369095	0.0797215
0.5771777	0.1288272	0.5906004	0.0784760
0.6442913	0.1203960	0.6577141	0.0743031
0.7114050	0.1075568	0.7114050	0.0686937
0.7583845	0.0960040	0.7583845	0.0620001
0.8187868	0.0781407	0.8187868	0.0506813
0.9060345	0.0466863	0.8859004	0.0340652
0.9463027	0.0300845	0.9463027	0.0149059
0.9664368	0.0213336	0.9664368	0.0075193
0.9865709	0.0122979	0.9798595	0.0022905
0.9932823	0.0092250	0.9865709	-0.0004172
0.9974000	0.0074000	0.9930000	-0.0027235
1.0000000	0.0046913	0.9950000	-0.0031000
1.0000000	0.0024000	0.9980000	-0.0022098
1.0000000	0.0000000	1.0000000	0.0000000

Table 3.1: Profile Coordinates [30]

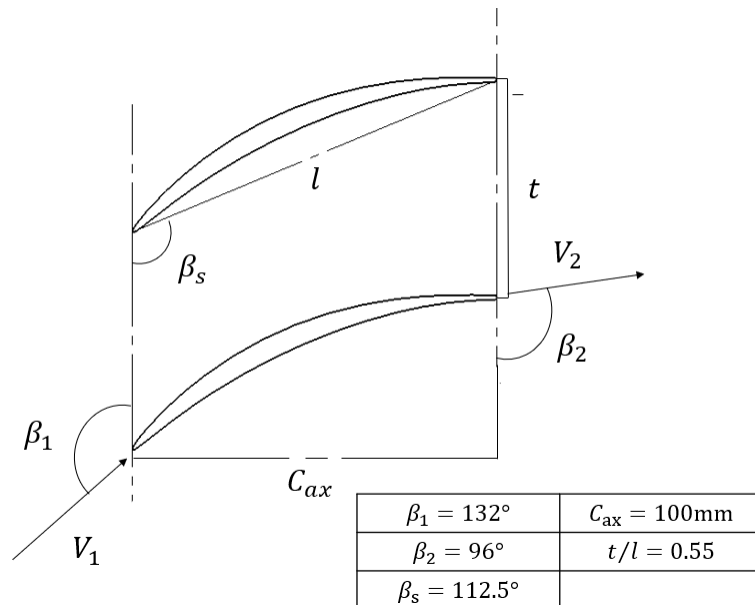


Fig 3.1: Compressor Cascade [30]

Compressor cascade was designed in 1971 by Hoheisel called V103-220. In this thesis, the axial chord of the compressor cascade is set to 100mm, and the installation angle of the cascade is consistent with V103-220. The inlet flow angle of the cascade is 132° and the outlet flow angle of the cascade is 96° . Besides, the ratio of blade spacing to blade chord is 0.55. By defining the length of axial chord, the size of the entire cascade is fully determined.

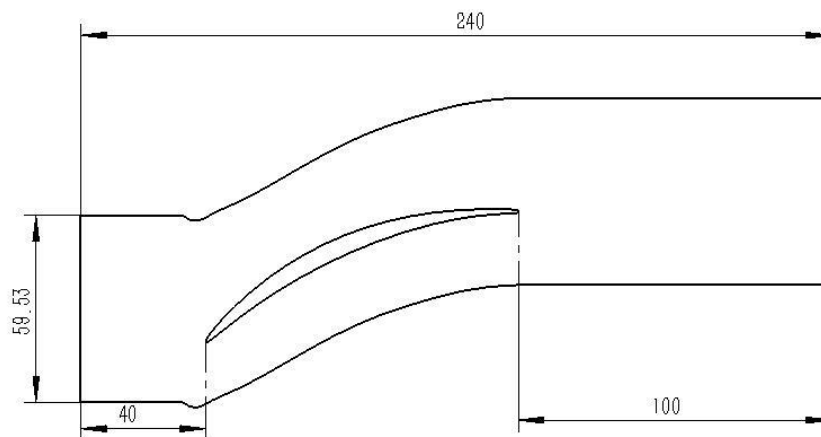


Fig 3.2: 2D single channel cascade

Since the cascade is a plane cascade, and the arrangement of the blades can be obtained in the form of an array. In order to simplify the calculation, save the calculation cost and calculation time, the calculation model used in this thesis is a single-channel two-dimensional cascade which is represented in Fig 3.2. The size of the inlet passage at the front of the blade cascade is 40mm, and the size of the outlet passage is 100mm.

3.2 Meshing

The model is built by SolidWorks, and the mesh is drawn by ICEM. Since ICEM cannot recognize the 2D model, the 3D model is created by SolidWorks which is presented in Fig 3.3. After importing into ICEM, the extruded part is deleted, and finally the plane mesh is drawn.

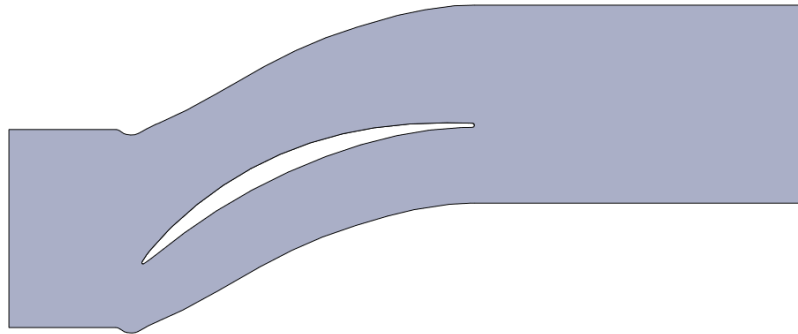


Fig 3.3: Cascade model created by SolidWorks

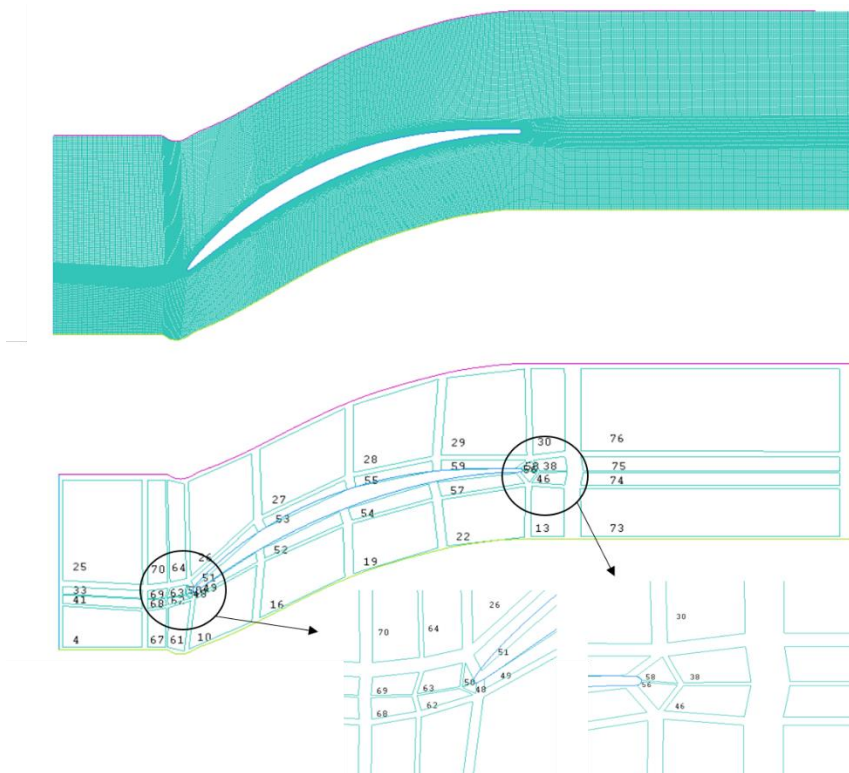


Fig 3.4: Example mesh and block structure

ICEM is used for mesh division. There are 76 blocks in the whole domain. O_Block is used to divide the surrounding of the blade, and the surface layer mesh is used to refine the surrounding of the blade to improve the accuracy of calculation. In Fig. 3.4, it can be seen that the leading edge and trailing edge of the blade are divided into more blocks

to improve the mesh quality, and the overall mesh quality is controlled above 0.85 and more than 95 percent of the mesh quality is equal to 1.

Since a single-channel cascade is used for numerical simulation, periodic grids need to be set in the grid. The period was set to be arrayed at 59.53 mm in the y-axis direction.

3.3 Numerical set up

In the present study, two-dimensional numerical simulations are performed by solving steady-state incompressible Reynolds-Averaged Navier-Stokes (RANS) equations and unsteady Reynolds-Averaged Navier-Stokes (URANS) equations.

3.3.1 Continuity and Momentum Equations

For all flows, ANSYS Fluent solves conservation equations for mass and momentum. For flows involving heat transfer or compressibility, an additional equation for energy conservation is solved. In this paper, incompressible fluids are used, so only the mass conservation equation and the momentum equation are considered. [31]

The Mass Conservation Equation:

$$\nabla \cdot (\rho \vec{v}) = 0 \quad (3.1)$$

Momentum Conservation Equations:

$$\frac{\partial}{\partial t} (\rho \vec{v}) + \nabla \cdot (\rho \vec{v} \vec{v}) = -\nabla p + \nabla \cdot \bar{\tau} \quad (3.2)$$

The stress tensor $\bar{\tau}$ is given by

$$\bar{\tau} = \mu [(\nabla \vec{v} + \nabla \vec{v}^T) - \frac{2}{3} \nabla \cdot \vec{v} I] \quad (3.3)$$

where μ is the molecular viscosity, I is the unit tensor, and the second term on the right side is the effect of volume dilation.

3.3.2 Turbulence

Solving turbulence problems is inseparable from the development and improvement of turbulence models.[32] After the rapid development of numerical simulation for decades, there are several classical turbulence models, which provide more help for people's more intuitive cognition, but these models further optimization is required to simulate more complex turbulent phenomena,[33][34] and this section will start with an introduction to the most classic turbulence models and in the following chapters, we will use various models for numerical simulation to select the most suitable turbulence model for low-velocity cascade simulation.[35][36]

Spalart-Allmaras Model

The Spalart-Allmaras model is a one-equation model that solves a modeled transport equation for the kinematic eddy (turbulent) viscosity. The Spalart-Allmaras model was designed specifically for aerospace applications involving wall-bounded flows and has been shown to give good results for boundary layers subjected to adverse pressure gradients and can be used to simulate turbulent separation and entropy generation. It is also gaining popularity in turbomachinery applications.[37][38][39]

The Spalart-Allmaras model is suitable for solving low Reynolds numbers and only for aerodynamic flows, but not for plane and round jet flows. The solution requires $1 < y^+ < 30$.

Shear-Stress Transport (SST) $k-\omega$ Model

For $k-\omega$ model, k represents the turbulence kinetic energy and ω represents the specific dissipation rate. The SST $k-\omega$ model includes all the refinements of the BSL $k-\omega$ model, and in addition accounts for the transport of the turbulence shear stress in the definition of the turbulent viscosity. Through continuous improvement of

the model, the use of the SST model to calculate a wider range of fluids has higher confidence and accuracy.[40][41][42]

Transition SST Model

The Transition SST model is based on the coupling of the SST $k - \omega$ transport equations with two other transport equations, one for the intermittency and one for the transition onset criteria, in terms of momentum-thickness Reynolds number. An ANSYS empirical correlation has been developed to cover standard bypass transition as well as flows in low freestream turbulence environments.

However, the Transition SST model can only calculate wall flows, not transition in free shear flows. In addition, the model cannot be applied to relatively moving walls and flow fields with zero freestream velocity. Of course, the model cannot superimpose other influencing factors, such as buoyancy and multiphase turbulence.[43][44][45]

k-kl- ω Transition Model

The $k - kl - \omega$ transition model is used to predict boundary layer development and calculate transition onset. This model can be used to effectively address the transition of the boundary layer from a laminar to a turbulent regime.[46][47][48]

3.3.3 Grid independence verification

In the process of numerical simulation, the final simulation results should not be affected by the number of grids. However, in order to save computing resources and speed up the calculation, the number of grids cannot be increased without limit. Therefore, selecting the appropriate number of grids is a process of numerical simulation critical step.

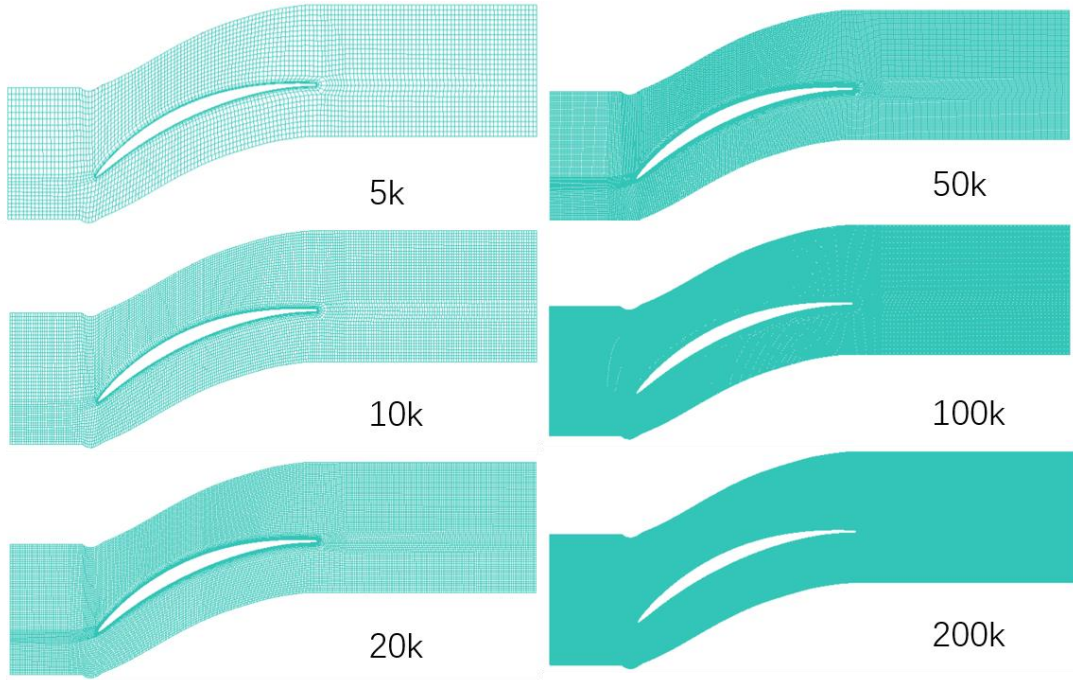


Fig 3.5: Grids with different numbers of nodes

Mesh	X direction nodes	Y direction nodes	Blade surface nodes
5k	153	30	150
10k	244	47	238
20k	326	73	320
50k	442	102	446
100k	710	159	702
200k	950	222	934

Table 3.2: Profile Coordinates

In table 3.2, the node distribution of the mesh is described in detail. When the number of meshes increases, the number of nodes in the X and Y directions and the blade surface increases. When the number of grids is 200k, the number of nodes in the X direction reaches 950, the number of nodes in the Y direction is 222, and the number of nodes on the blade surface is 934.

$$y^+ = yu_\tau/\nu \quad (3.4)$$

Pressure coefficient:

$$C_p = (P - P_{ref}) / (0.5\rho V_{ref}^2) \quad (3.5)$$

Friction coefficient:

$$C_f = \tau / (0.5\rho V_{ref}^2) \quad (3.6)$$

Total pressure loss coefficient:

$$\phi = (p_{0,in} - p_{0,out}) / p_{0,in} \quad (3.7)$$

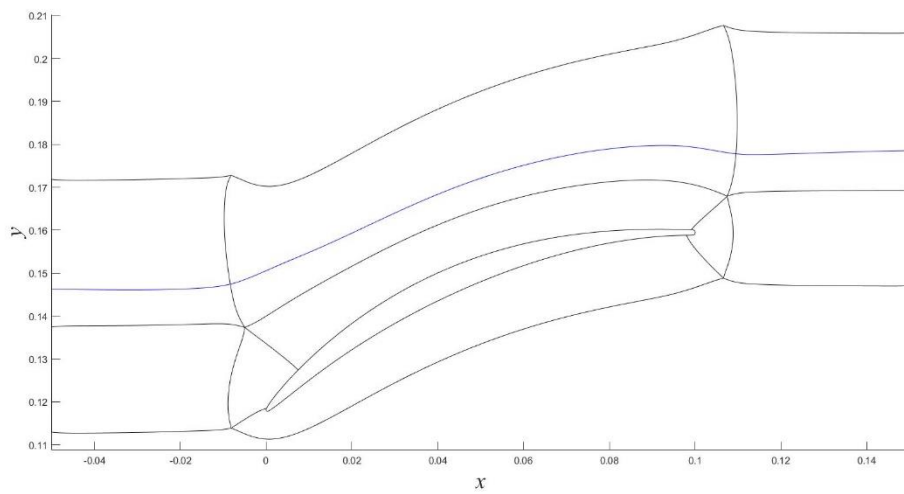


Fig 3.6: Block division of DNS and drawing line of turbulence intensity

Figure 3.6 describes the meshing of DNS, in which there are 9 blocks in DNS and 4 blocks around the surface of the blade. The inlet length is 0.5 times C_{ax} , and the outlet is 0.15 times C_{ax} . The blue curve is selected as the research curve for turbulence intensity, and the curve at the same position is also selected in Fluent to compare the changes of turbulence intensity at the same position.

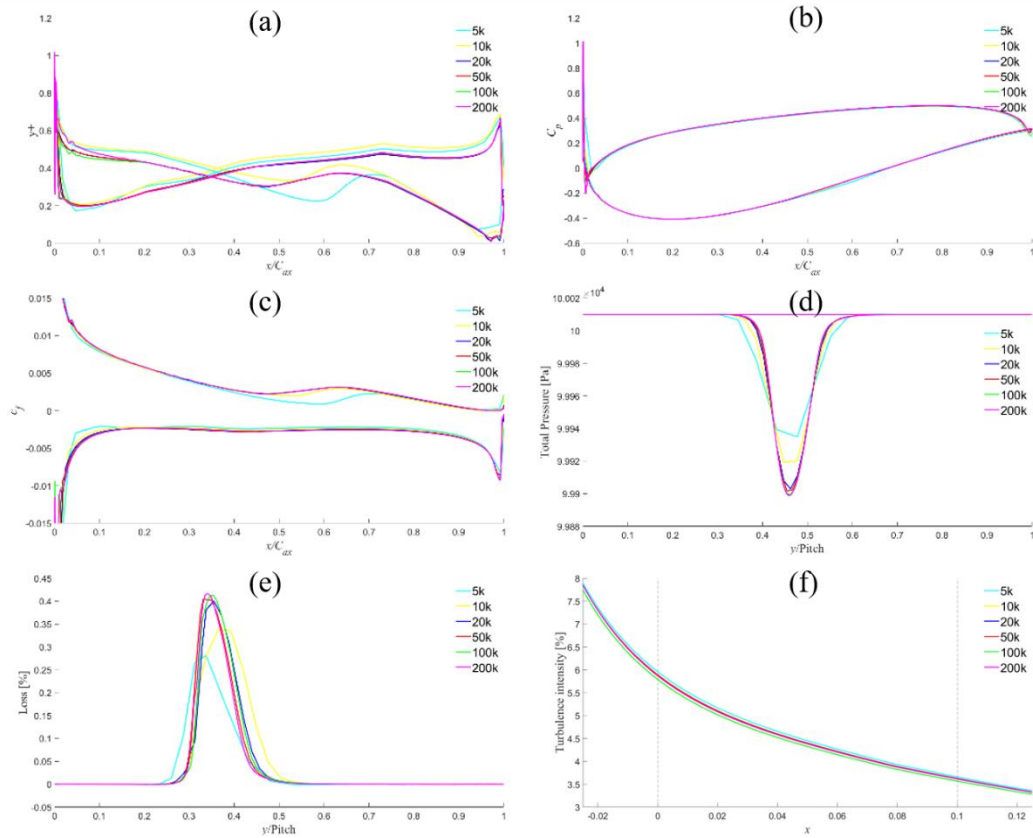


Fig 3.7: Grid independence verification comparison

Figure 3.7(a) shows the distribution of different grid numbers y^+ , which is less than 1 on the whole, at most positions is about 0.4, and y^+ is the largest at the leading edge position, with a value of about 1. But different grids correspond to the y^+ is very similar, except that the grid with a grid number of 5k is quite different from the other grids, and the other grids have only very small differences.

In Figure 3.7(b), each grid has the same pressure coefficient, except that the grid with a grid number of 5k has a small difference in the leading edge position. Figure 3.7(c) shows the skin friction coefficient of different grids. In the middle of the blade, the grids with fewer nodes are significantly different from other grids, and the other grids are basically the same. Figure 3.7(d) shows the total inlet and outlet pressures. It is obvious that at the inlet, the total pressure is a constant value along the y -axis and there is no difference between each grid. Compared with the inlet total pressure, the outlet total

pressure has an obvious pressure drop locally, but the minimum pressure of the grid with a grid number of 5k is higher than that of other grids, followed by the grid with a grid number of 10k. The rest of the grids have the same pressure distribution. Figure 3.7 (e) has the opposite trend compared to (d), the grid with 5k nodes has the largest total pressure loss. The variation of Tu along the flow direction is described in Figure 3.7 (f), and there is no significant difference between the six grids.

Through comprehensive comparative analysis, a grid with a node number of 50k is finally selected as the calculation grid. There is no obvious difference between this grid and a grid with a higher number in the comparison of various parameters. In the case of ensuring the calculation accuracy, the calculation velocity is also improved, and the calculation time is saved.

3.3.4 Turbulence Model Comparison

This section will compare the results of five RANS simulations with DNS, where DNS is direct numerical simulation, $k\omega$ is k-omega model, SA is Spalart-Allmaras model, Tk is Transition k-k-kl-omega model, TS is Transition SST model and $k\omega T$ is k-omega model with transition options.

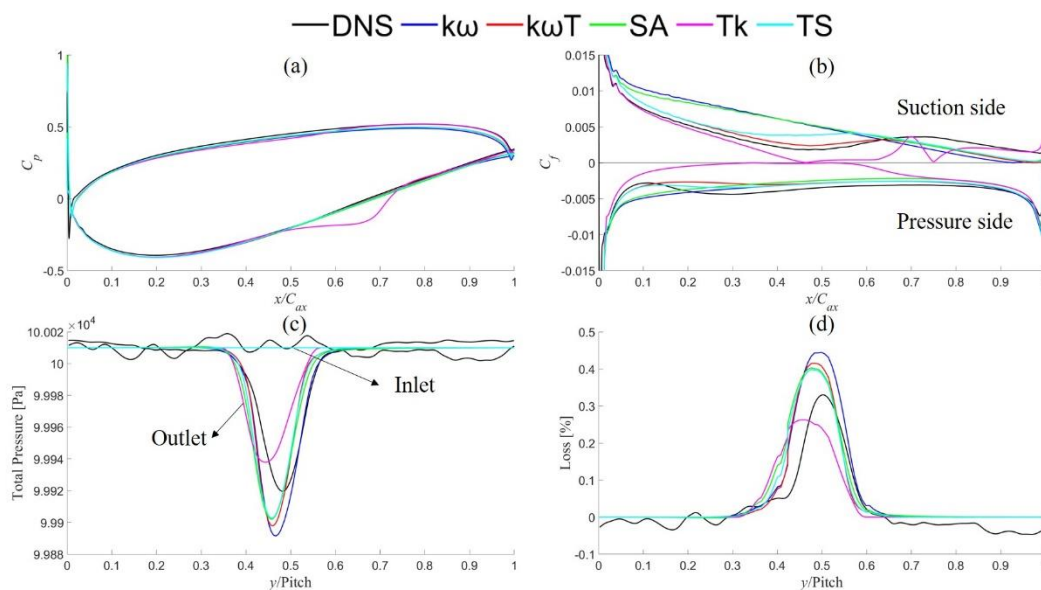


Fig 3.8: Turbulence Model Comparison

In figure 3.8(a), the effect of the turbulence model on the pressure coefficient is compared. The results obtained by the Transition k-k-kl-omega model are quite different from other turbulence models. The separation phenomenon occurs in the middle and lower position of the blade suction side, while the calculation results of other turbulence models are basically consistent with DNS. Figure 3.8(b) shows the skin friction coefficient of different turbulence models. On the pressure side, except that the results of Tk model are quite different from DNS, the calculations of other turbulence models are basically same. For the DNS results, it can be seen that there is an obvious trend of rising firstly and then falling. Although the curves of the pressure side overlap well on the whole, the results of each RANS turbulence model do not have this trend. The results of the various turbulence models on the suction side are significantly different. The curves of $k\omega$ and SA model basically overlap, and the same decline rate is basically maintained from the leading edge to the trailing edge, but there is a big difference with the results of DNS. After the Tk model showed separation in the second half of the blade, the curve became abnormally fluctuating, which was the most different from the DNS results. The $k\omega T$ and TS models have the same trend as the DNS results, but there are still some differences between the TS model and DNS in the middle part of the blade, but the $k\omega T$ model and DNS results are highly similar.

In Figure 3.8 (c), the total pressure distributions at the inlet and outlet of the DNS are compared for each turbulence model. For the inlet total pressure, it is very obvious that the curve of the total inlet pressure of DNS is not a straight line, it fluctuates around 100010 Pa, which is like the actual pressure distribution, while several turbulence models of RANS are limited by grids and so on. For the total pressure at the outlet, after the airflow passes through the blade, an obvious wake area will be generated. In this area, the total pressure will be lower than other areas, and the pressure distribution will be in the form of a quadratic function. The total pressure loss obtained by the Tk model is significantly larger than that of DNS, but the total pressure obtained by other models

is slightly smaller than that of DNS. In addition, due to the effect of separation, the wake area obtained by the Tk model has a certain deviation from several other models. Figure 3.8(d) shows the distribution of the total pressure loss, which has an opposite distribution trend to the total pressure distribution.

The calculation results of the $k\omega T$ and TS model are the most similar to the DNS in the comparison of various parameters. Therefore, the $K\omega T$ and TS model is finally used as the turbulence model for the following research.

4 Result and discussion

4.1 Steady case

4.1.1 Compared with DNS with Tu equals to 6%

In order to make the RANS result match the DNS result better, this part selects the inlet condition which is same with the DNS result by modifying the turbulence intensity of of the inlet and comparing it with the DNS result.

The model selected first is the k- ω model with transition options, the inlet condition is the total pressure inlet, $P_I^* = 100010$ Pa and the outlet is the natural outflow. Select 3%、5%、7%、9% and 10% for the turbulence intensity of the inlet.

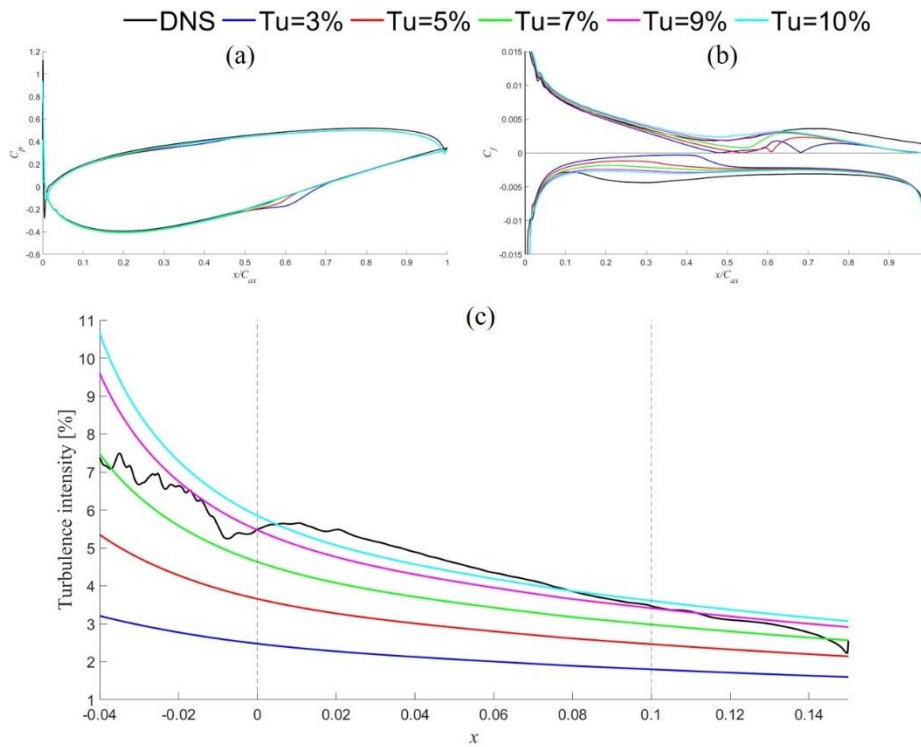


Fig 4.1: Comparison of turbulence intensity between DNS (Tu=6%) and k-omega model with transition options

Turbulence Intensity [%]	IP_0 [Pa]	I_p [Pa]	OP_0 [Pa]	Op [Pa]
3	100010	99738	100000	99847
5	100010	99739	100000	99847
7	100010	99739	100000	99847
9	100010	99740	100000	99847
10	100010	99740	100000	99847
DNS_Tu=6%	100010	99736	100000	99849

Table 4.1: Comparison of parameters under different inlet turbulence intensity between DNS(Tu=6%) and k-omega model with transition options

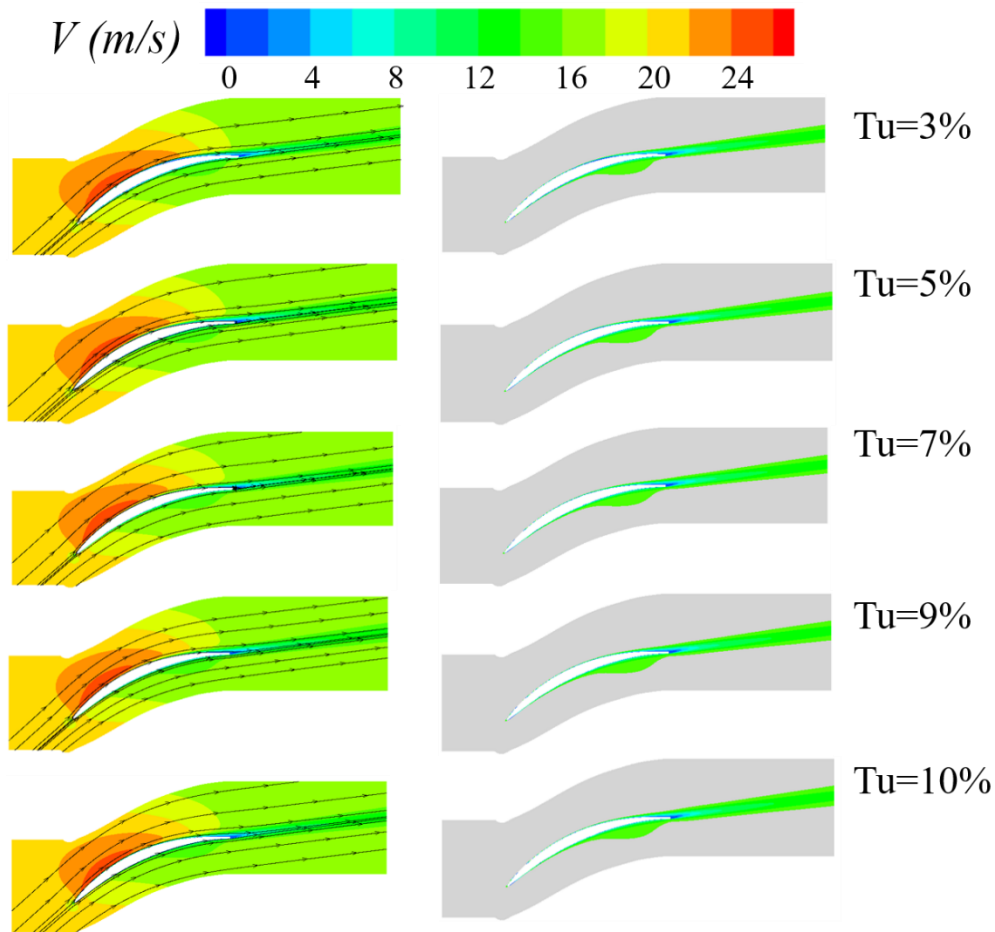


Fig 4.2: Comparison of velocity and boundary layer of k-omega model with transition options under different turbulence intensities (higher turbulence intensity)

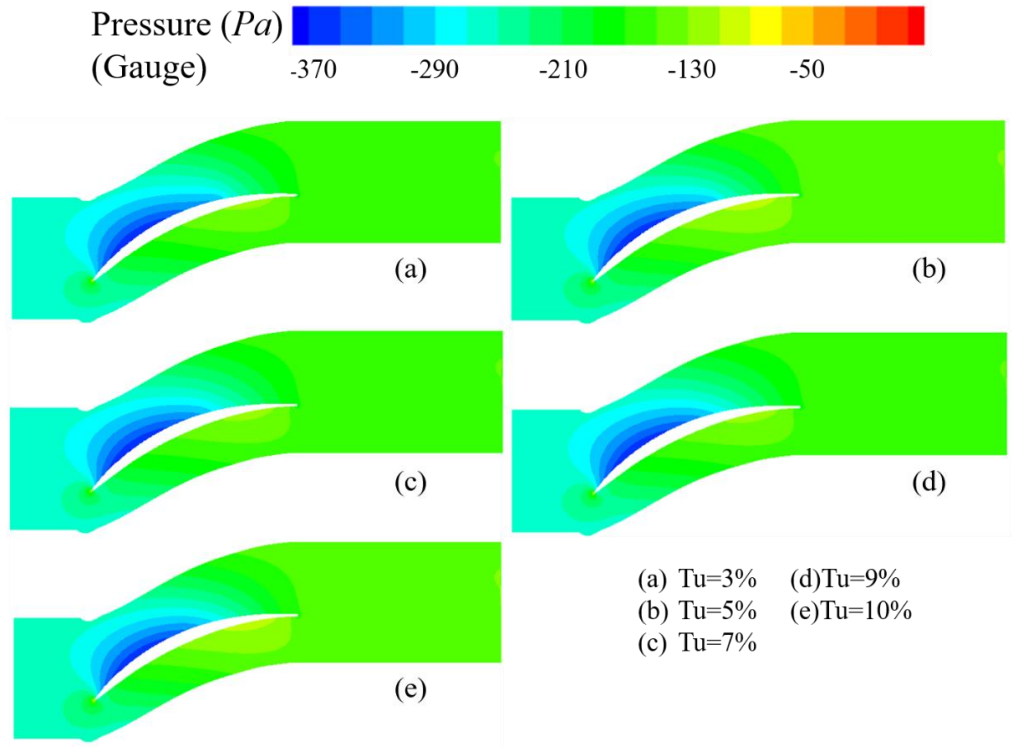


Fig 4.3: Comparison of static pressure of k-omega model with transition options under different turbulence intensities (higher turbulence intensity)

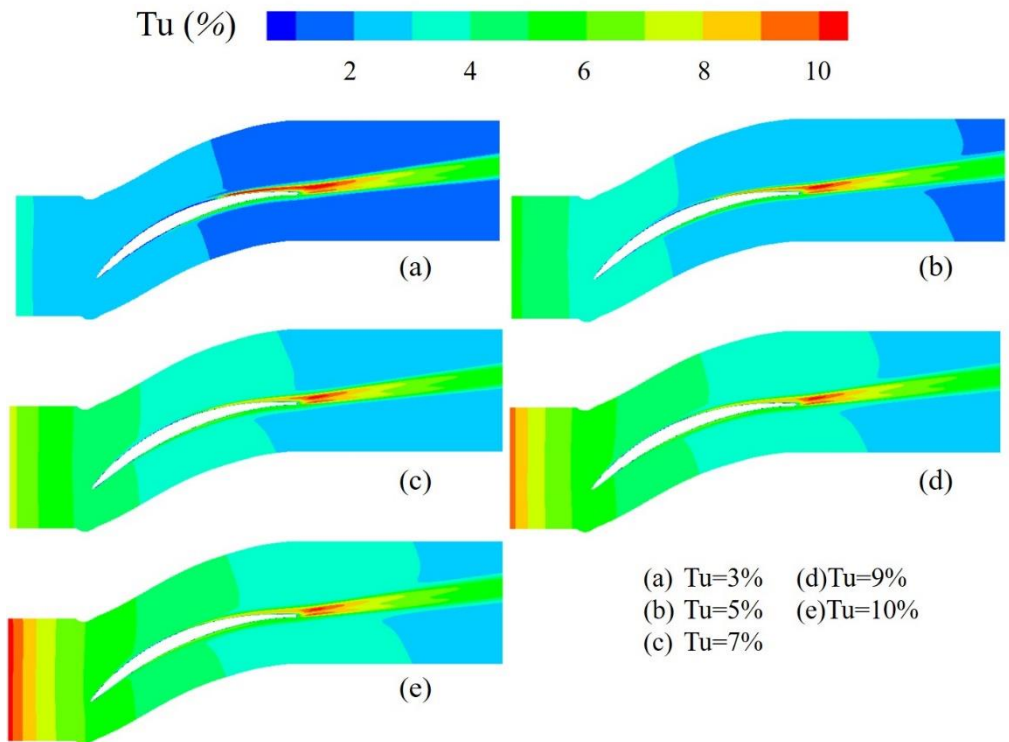


Fig 4.4: Comparison of turbulence intensity of k-omega model with transition options under different turbulence intensities (higher turbulence intensity)

In order to keep the changing trend of turbulence intensity of RANS as consistent as DNS, the inlet turbulence intensity of the calculation model was modified, and the pressure coefficient and skin friction coefficient were compared.

Figure 4.1 shows that when the turbulence intensity of the RANS is low, a separation occurs in the middle of the suction side, but as the inlet turbulence intensity increases, the range of separation becomes smaller and smaller, which tends to be consistent with the results of DNS. For skin friction coefficient, there are obvious fluctuations at the pressure side due to the influence of separation, but with the increasement of turbulence intensity, the fluctuation tends to be flat, and the coincidence with DNS increases significantly. At the front of pressure side, as the turbulence intensity increases, the values of RANS and DNS tend to be more consistent. From the distribution curve of turbulent lightness, it can be seen that at the inlet position, the turbulence intensity obtained by RANS decreases significantly faster than that of DNS. When the turbulence intensity is 10%, the results of RANS and DNS are the most similar. Due to the accuracy of the calculation, the turbulence of the RANS has always shown a downward trend, while the DNS has some fluctuations, but the overall trend is downward. Especially at the front of the inlet, the turbulence intensity has an obvious trend of change, but this trend cannot be reflected in RANS. When calculating with this model, compared with DNS, RANS needs to increase the turbulence intensity of the inlet appropriately to solve the problem that the turbulence intensity at the inlet decreases rapidly.

Table 4.1 shows that the total pressure at the inlet remains constant for different turbulence intensities. Compared with the DNS data, the static pressure at the RANS inlet is slightly larger, and the greater the turbulence intensity, the bigger static pressure at the inlet. DNS and RANS have the same total outlet pressure, but the outlet static

pressure gap is slightly larger than the data of RANS, but the outlet static pressure of RANS remains the same under various working conditions, all of which are 99847Pa. Figure 4.2 shows the velocity distribution and boundary layer for different turbulence intensities when using the k-omega model with transition options. It is obvious that the distribution of the resting velocity contour is basically same. On the suction side, a region with relatively high local velocity is generated, and then the velocity decreases. On the pressure side, the velocity shows a slow downward trend, and there is no velocity fluctuation. A relatively obvious change is that with increasing turbulence intensity, the location of the high-velocity region is relatively far from the inlet location, but the difference is not very big. The flow field can also be seen from the distribution of the boundary layer. At the trailing edge of the pressure side, there is a relatively large low-velocity area, and after passing through the blade, there is a wake area along the direction of the blade. Changes in turbulence intensity did not significantly change the velocity distribution.

Figure 4.3 describes the pressure distribution of the entire domain. Corresponding to figure 4.3, a local low pressure area is formed in the area with high velocity, and a local high pressure area is formed at the trailing edge of the pressure side. With the change of turbulence intensity, the pressure distribution is also basically the same.

Figure 4.4 compares the distribution of turbulence intensity across the domain. There is a very obvious decrease in the turbulence intensity at the inlet. The bigger turbulence intensity at the inlet, the more obvious the decrease at the inlet. Due to the influence of the wake, a well-defined region of high turbulence intensity is formed at the outlet. On the whole, the turbulence intensity is decreasing continuously, but the decrease is the fastest at the inlet.

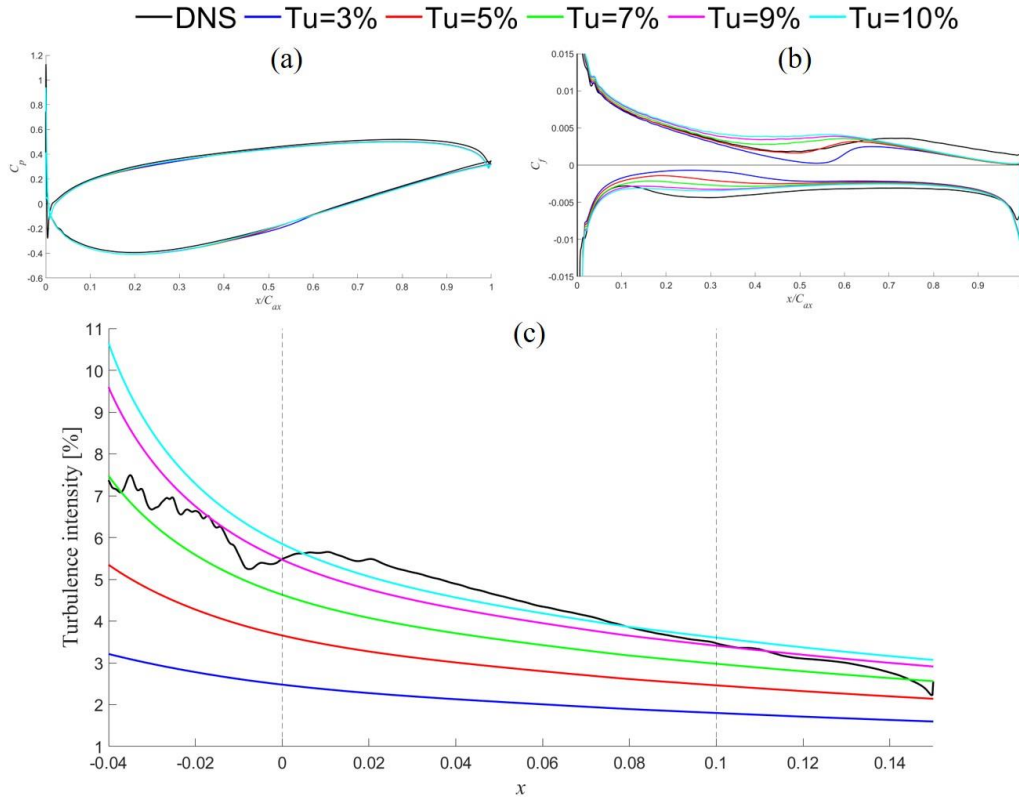


Fig 4.5: Comparison of turbulence intensity between DNS (Tu=6%) and Transition SST model

Turbulence Intensity [%]	IP ₀ [Pa]	Ip [Pa]	OP ₀ [Pa]	Op [Pa]
3	100010	99738	100000	99847
5	100010	99739	100000	99847
7	100010	99739	100000	99847
9	100010	99740	100000	99847
10	100010	99740	100000	99847
DNS_Tu=6%	100010	99736	100000	99849

Table 4.2: Comparison of parameters under different inlet turbulence intensity between DNS(Tu=6%) and Transition SST model

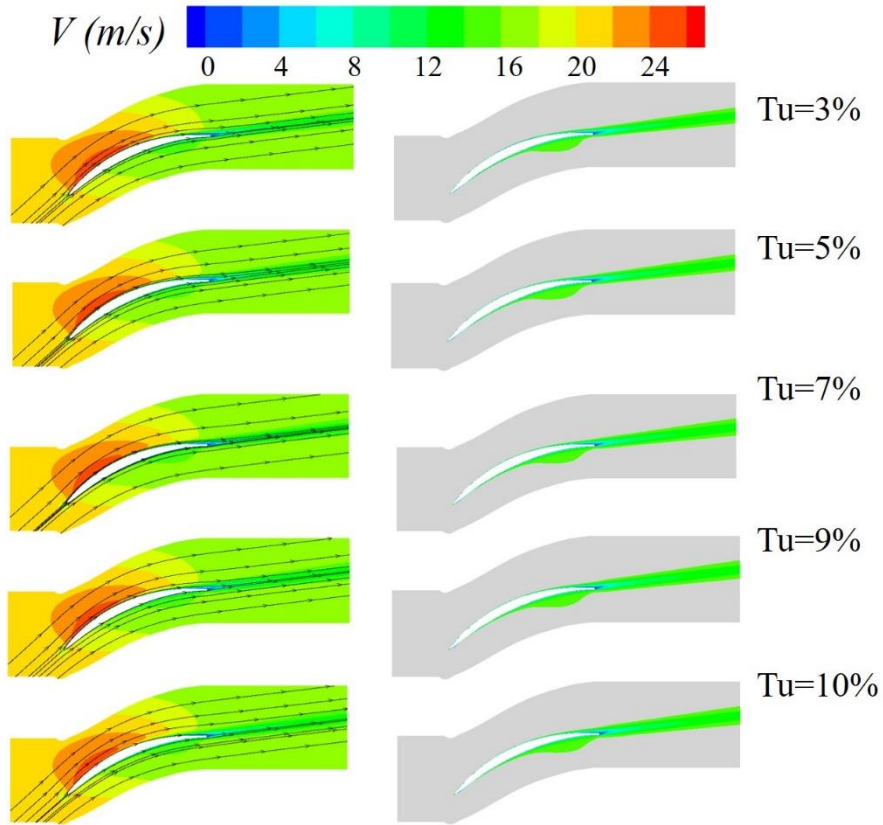


Fig 4.6: Comparison of velocity and boundary layer of Transition SST model under different turbulence intensities (higher turbulence intensity)

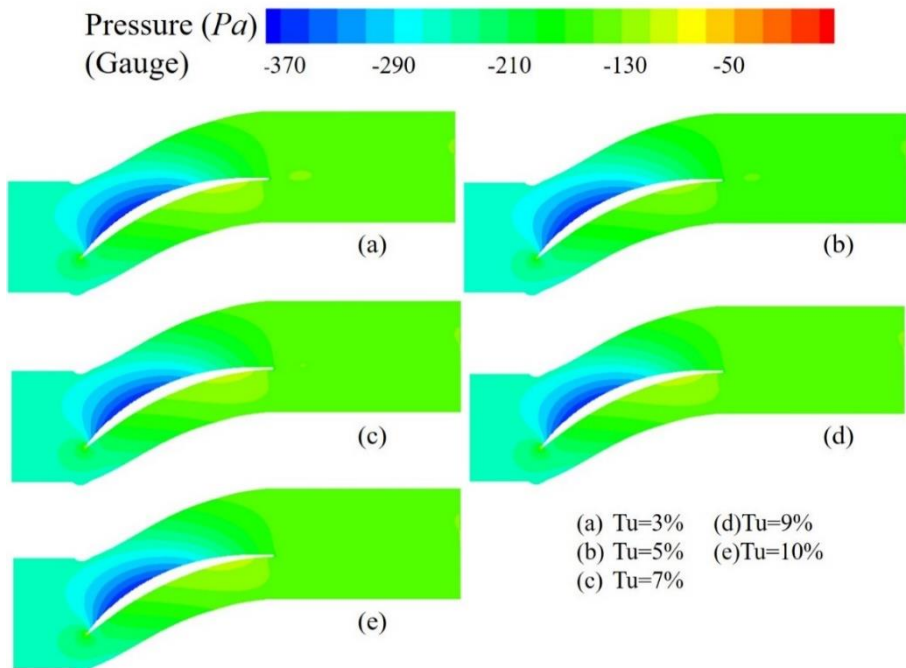


Fig 4.7: Comparison of static pressure of Transition SST model under different turbulence intensities (higher turbulence intensity)

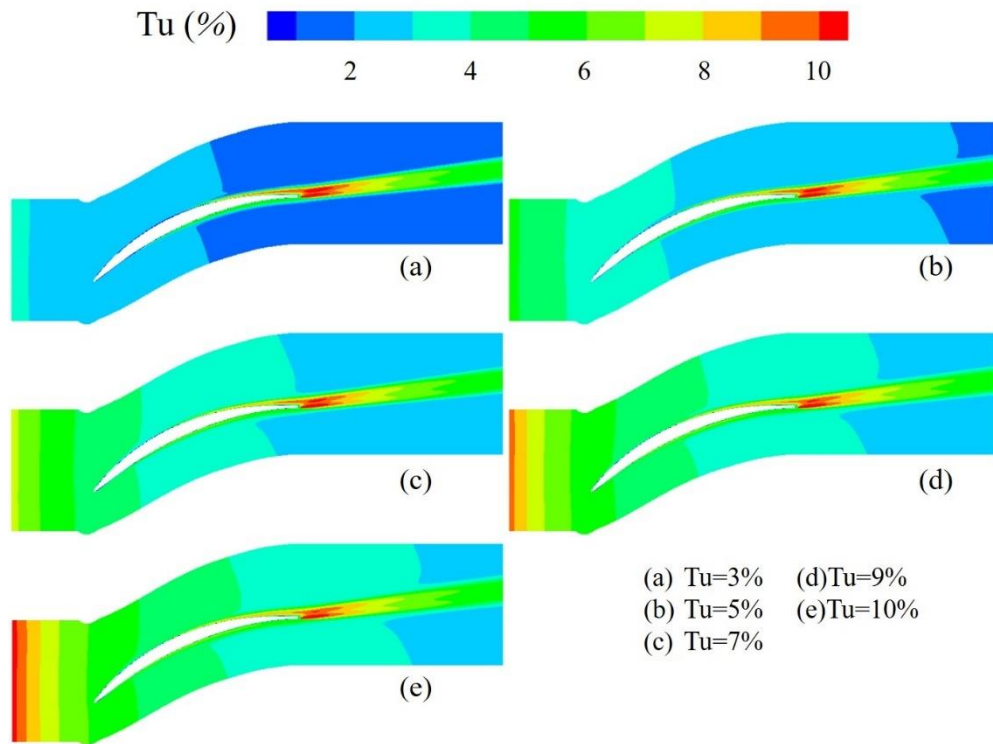


Fig 4.8: Comparison of turbulence intensity of Transition SST model under different turbulence intensities (higher turbulence intensity)

Figure 4.5 shows a comparison of DNS and RANS results when using the Transition SST model. In Figure 4.5(a), the pressure coefficient fluctuates slightly except for the middle position of the suction side, and there is almost no difference in other positions. The skin friction coefficient shown in 4.5(b) is quite different. For the suction side, at the leading edge position, the curve of RANS and DNS have a good coincidence, but there is a big difference in the middle part. With the increasement of inlet turbulence intensity, the skin friction coefficient gradually increases. When the turbulence intensity is 5%, the curves of RANS and DNS have the best coincidence. At the trailing edge of the blade, the coefficient values corresponding to different turbulence intensities are basically same, but they are all smaller than the value of DNS. When compare the turbulence intensity, along the flow direction, the turbulence intensity becomes smaller, and when the turbulence intensity is 9%, the change curve of the RANS turbulence intensity is the closest to the DNS.

Table 4.2 shows that the total inlet pressure corresponding to different inlet conditions is consistent with the total inlet pressure of DNS, and the static pressure at the inlet position increases with the increasement of turbulence intensity, of which the minimum is 99738Pa and the maximum is 99740Pa, the inlet static pressure corresponding to DNS is 99736Pa, which is closest to the DNS result when the turbulence intensity at the inlet position is 3%. Similarly, the total pressure of each outlet remains the same, which is 100000Pa, and the outlet static pressure corresponding to RANS is also the same, which is 99847Pa, is 2Pa smaller than the outlet static pressure corresponding to DNS of 99849Pa.

Figure 4.6 depicts the velocity distribution and boundary layer distribution when using the Transition SST model, and Figure 4.7 depicts the pressure distribution when using the Transition SST model. Figure 4.8 depicts the turbulence intensity distribution using the Transition SST model. Much like when using the k-omega model with transition options, it's hard to tell the difference.

4.1.2 Compared with DNS with Tu equals to 4%

In order to compare RANS and DNS more comprehensively, this section will compare the RANS results and DNS results with 4% turbulence intensity at the inlet.

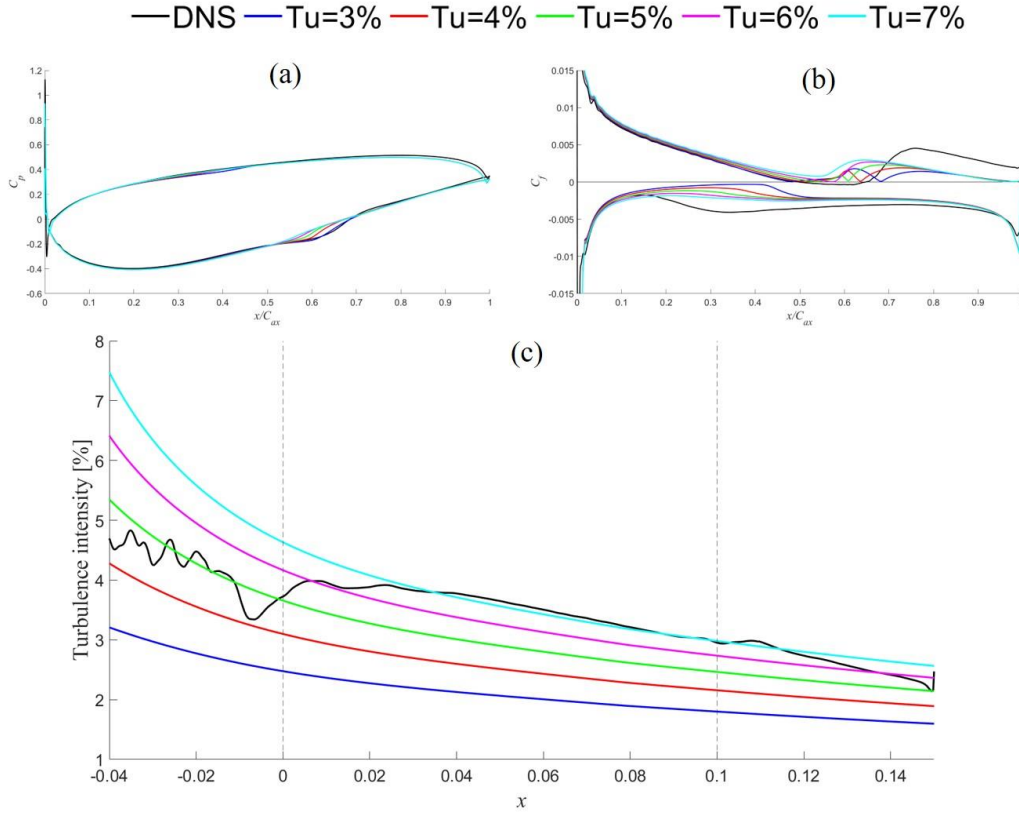


Fig 4.9: Comparison of turbulence intensity between DNS (Tu=4%) and k-omega model with transition options

Turbulence Intensity [%]	IP ₀ [Pa]	Ip [Pa]	OP ₀ [Pa]	Op [Pa]
3	100010	99739	100000	99847
4	100010	99738	100000	99847
5	100010	99738	100000	99847
6	100010	99739	100000	99847
7	100010	99739	100000	99847
DNS_Tu=4%	100010	99737	100000	99849

Table 4.3: Comparison of parameters under different inlet turbulence intensity between DNS(Tu=4%) and k-omega model with transition options

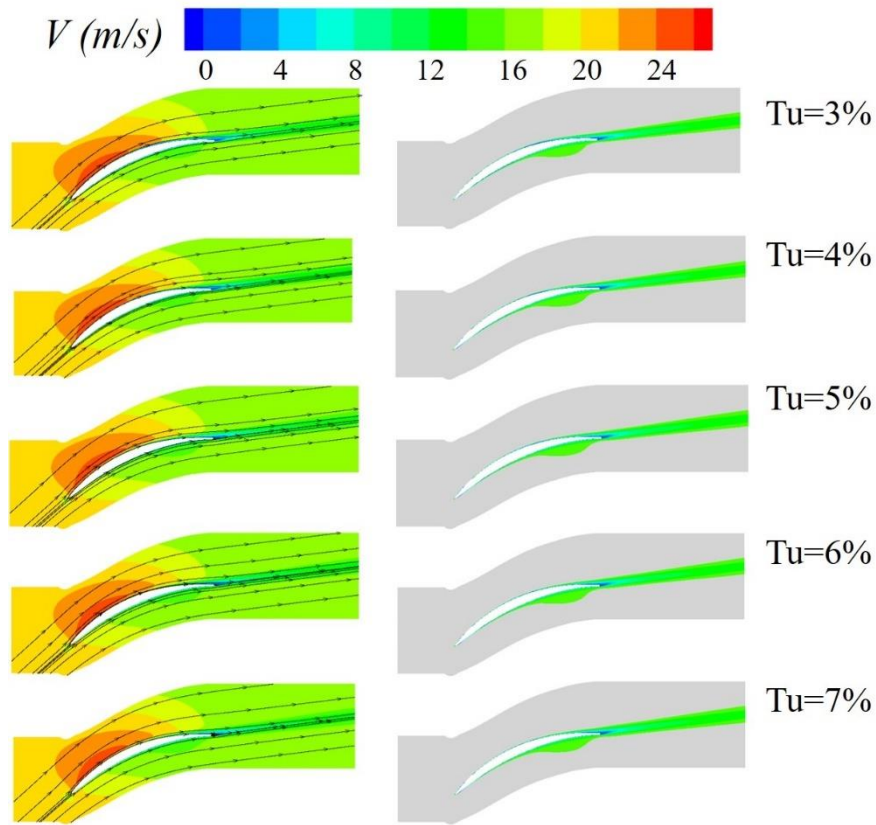


Fig 4.10: Comparison of velocity and boundary layer of k-omega model with transition options under different turbulence intensities (lower turbulence intensity)

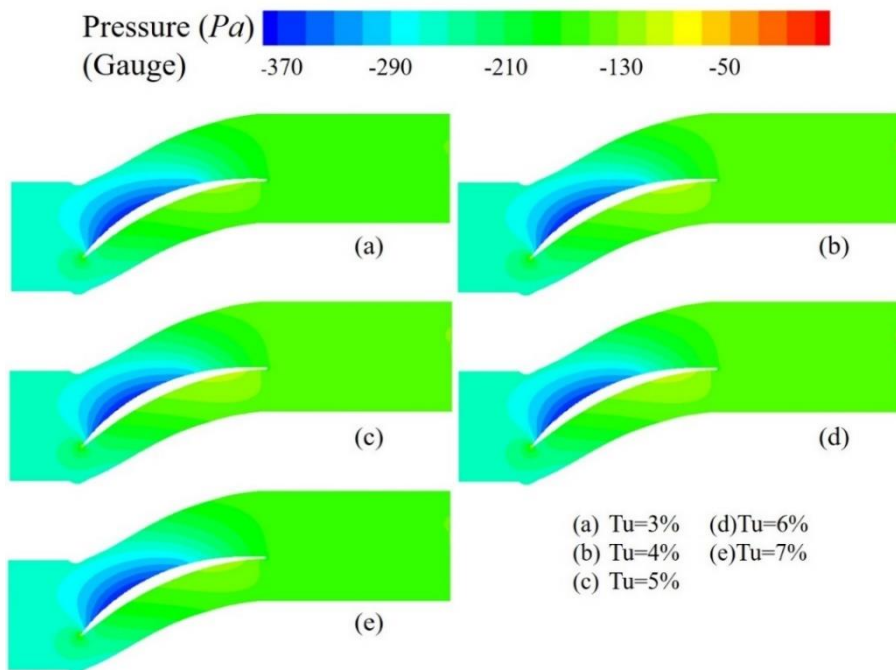


Fig 4.11: Comparison of static pressure of k-omega model with transition options under different turbulence intensities (lower turbulence intensity)

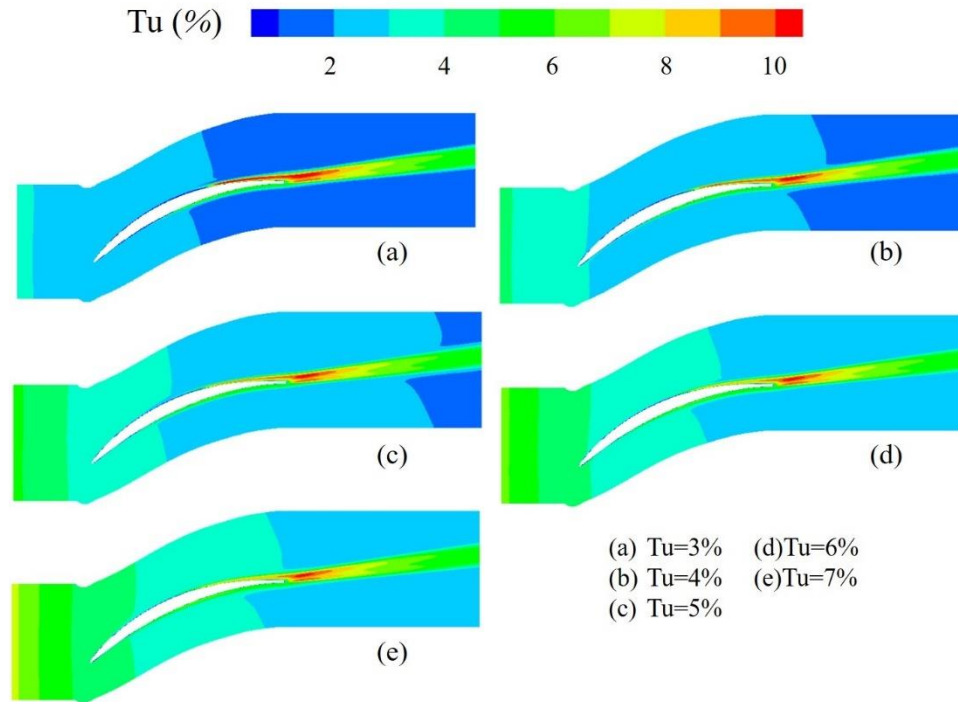


Fig 4.12: Comparison of turbulence intensity of k-omega model with transition options under different turbulence intensities (lower turbulence intensity)

Figure 4.9(a) shows that when the turbulence intensity at the DNS inlet is 4%, there is an obvious bubble on the suction side, which means that a separation occurs at this position. In contrast to the RANS data, as the turbulence intensity increases from 3% to 7%, the bubble formed at this position become smaller and smaller. When the turbulence intensity is 3%, the curves can overlap well, but when the turbulence intensity increases to 7%, there is no obvious bubble. In the front position of the suction side, the pressure coefficient is slightly different, but the overall trend remains the same. In Figure 4.9(b), there is a big difference in the skin friction coefficient of the suction side, especially in the middle position. When the skin friction coefficient drops to 0, the DNS data has a large increasement and then slowly. For the RANS curve, the amplitude of the increasement is much smaller than that of the DNS, and the position of the increasement is a little earlier than that of the DNS. Although the trailing edge has a similar downward trend, the overlap of the curves is small. Especially as the turbulence intensity decreases, the coincidence of the curves gradually becomes smaller. Among

them, the turbulence intensity is 3%, and the RANS curves of 4% and 5% fluctuate to a certain extent, and the difference with DNS is further increased. For the pressure side, the difference between DNS and RANS is mainly reflected in the front position in the middle. Here, the curve of DNS has a relatively obvious downward trend, while for the curve of RANS, it basically maintains a relatively level. When it develops to the middle position, the curves tend to overlap, and as the turbulence intensity decreases, the difference between RANS and DNS increases continuously. In Fig. 4.9(c), the distribution of turbulence intensity along the flow direction is compared. There is a high degree of similarity with the previous results. The turbulence intensity of DNS is fluctuating and decreasing, while the turbulence intensity of RANS is decreasing monotonically, and the RANS result with an inlet turbulence intensity of 7% is the most similar to the DNS result.

Table 4.3 shows that the total inlet pressure and the total outlet pressure are consistent under various working conditions. For the inlet static pressure, which of RANS is about 99738Pa or 99739Pa, is slightly larger than the inlet static pressure of DNS 99737Pa, while the outlet static pressure of RANS is about 99847Pa, which is slightly lower than the static pressure of DNS at 99849Pa.

Figure 4.10 compares the velocity contour at relatively low turbulence intensities, which are consistent with higher turbulence intensities. Similarly, Figure 4.11 has the same distribution law. It can be found in Figure 4.12 that when the turbulence intensity is small, the turbulence intensity decreases very slowly, and the trailing edge has a similar turbulence intensity distribution law, and not affected by the inlet turbulence intensity.

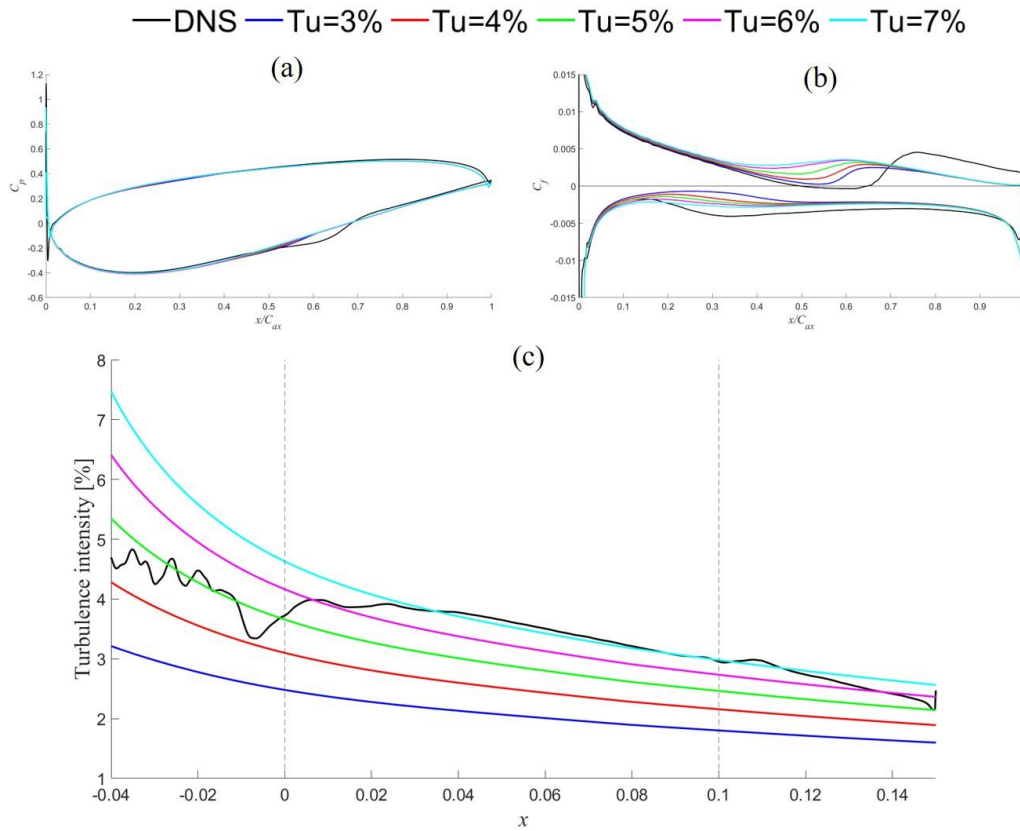


Fig 4.13: Comparison of turbulence intensity between DNS (Tu=4%) and Transition SST model

Turbulence Intensity [%]	IP_0 [Pa]	Ip [Pa]	OP_0 [Pa]	Op [Pa]
3	100010	99738	100000	99847
4	100010	99738	100000	99847
5	100010	99739	100000	99847
6	100010	99739	100000	99847
7	100010	99739	100000	99847
DNS_Tu=4%	100010	99737	100000	99849

Table 4.4: Comparison of parameters under different inlet turbulence intensity between DNS(Tu=4%) and Transition SST model

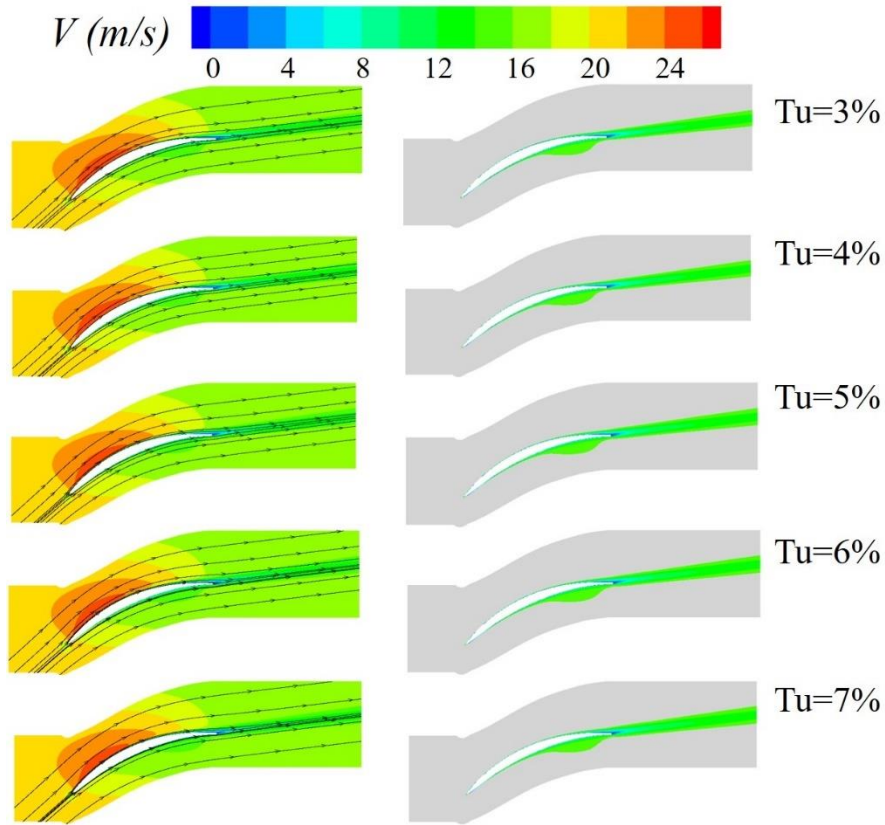


Fig 4.14: Comparison of velocity and boundary layer of Transition SST model under different turbulence intensities (lower turbulence intensity)

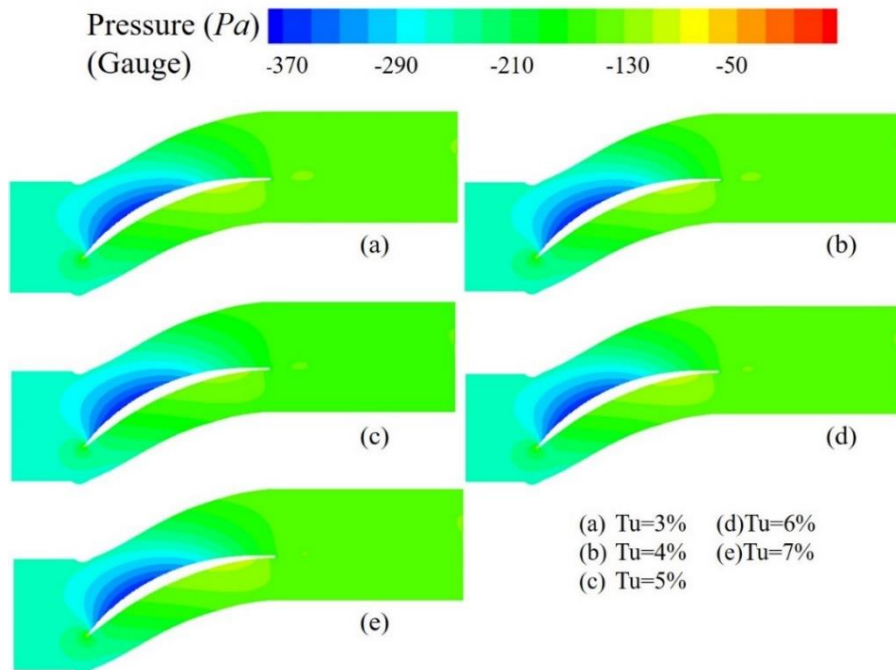


Fig 4.15: Comparison of static pressure of Transition SST model under different turbulence intensities (lower turbulence intensity)

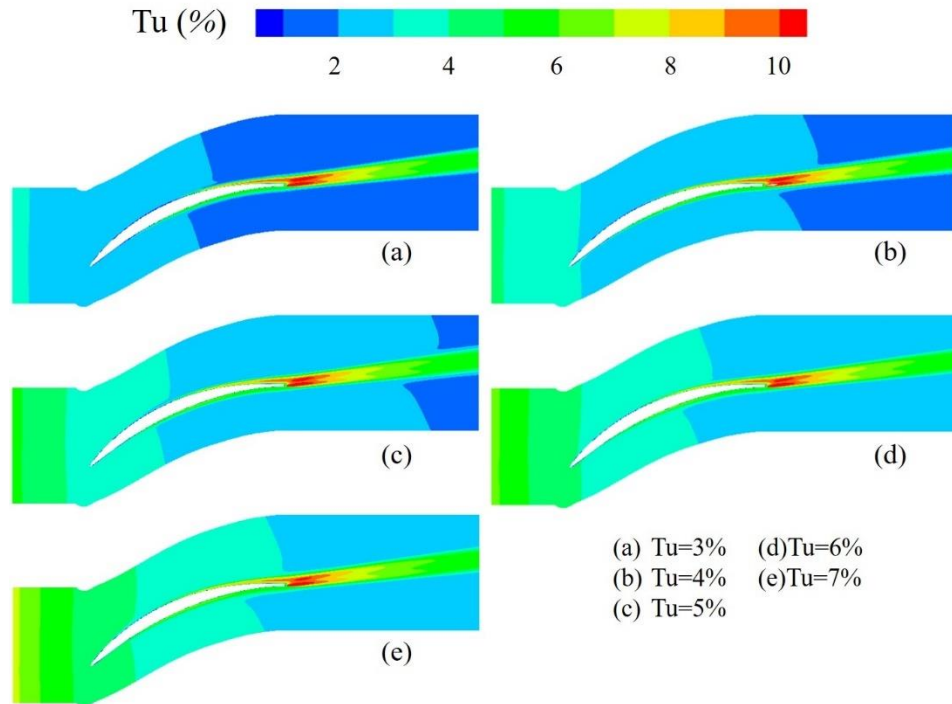


Fig 4.16: Comparison of turbulence intensity of Transition SST model under different turbulence intensities (lower turbulence intensity)

Figure 4.13(a) shows the comparison between the results of RANS and DNS when using the Transition SST model. It is very obvious that RANS does not form bubbles on the suction side, and the curve is relatively smooth, which is significantly different from the DNS curve. The coincidence of the position curves is very well. Figure 4.13(b) shows the difference in the skin friction coefficient. Similar to the above description, there is a significant difference in the middle position of the suction side. The RANS skin friction coefficient curve rises less than DNS, and the rising position is relatively forward, resulting in poor coincidence of the curves. The difference of the pressure side is much smaller. Although the overall trend is very similar, the absolute value of the RANS skin friction coefficient is still slightly smaller than that of DNS in the relatively forward position. The greater the turbulence intensity of the RANS, the greater the difference. Figure 4.13(c) shows the distribution curve of the turbulence intensity. The turbulence intensity of RANS decreases very rapidly. In the region with blades, the RANS with a turbulence intensity of 7% has the most similar results with DNS.

In Table 4.4, the data of the total inlet pressure and the total outlet pressure are consistent. The inlet static pressure of RANS is 99738Pa or 99739Pa, which is slightly larger than the DNS inlet static pressure of 99737Pa. The outlet static pressure of RANS is 99847Pa, which is slightly smaller than that of DNS, which is 99849Pa.

Figure 4.14, Figure 4.15 and Figure 4.16 are all consistent with the distribution law described above, and will not be introduced in detail.

4.1.3 Defining boundary conditions using UDF

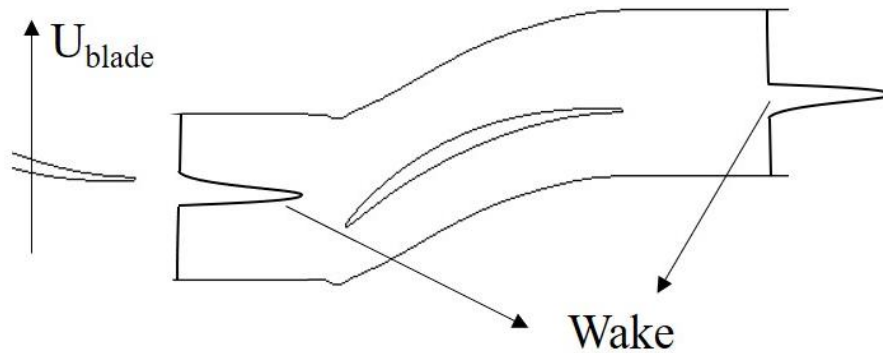


Fig 4.17: Schematic of the computational domain and wake recycling procedure

In order to simulate the intake situation of the multi-stage compressor more accurately, the blades are mirrored along the X-axis, and the pressure at the outlet is applied to the inlet position to make it more in line with the actual working conditions.

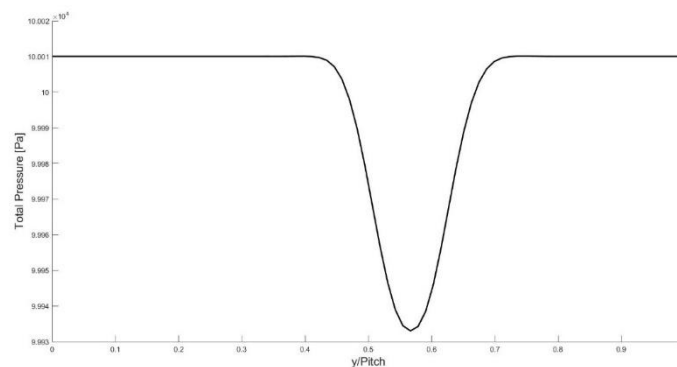


Fig 4.18: Inlet total pressure for steady case

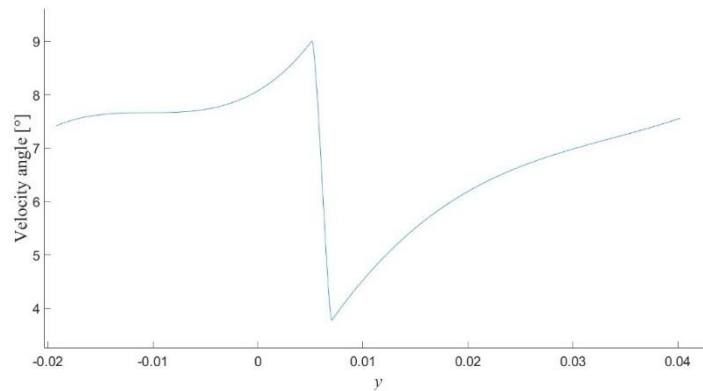


Fig 4.19: Outlet velocity angle

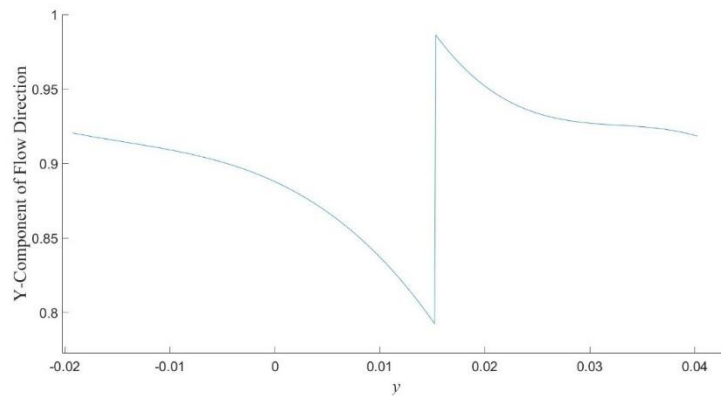


Fig 4.20: Y-Component of Flow Direction

As shown in Figure 4.18, the pressure at the outlet is mirrored and applied at the inlet, and the angle of the outlet is applied to the inlet in the same way. It is very obvious that there is a very pronounced dip in pressure due to the effect of the wake, and there is a following change in the angle of the outlet. Figure 4.19 shows the velocity angle of the outlet, mirrored along the X axis and then applied to the inlet position.

$$\theta_{Inlet} = \theta_{Outlet} - \overline{\theta_{Outlet}} + 42^\circ \quad (4.1)$$

A series of changes are required before the velocity angle of the outlet is applied to the inlet. Because the velocity angle of the outlet is already far less than 42° , it is necessary to subtract the average value of the velocity angle of the outlet and plus 42° before it

can act on the inlet position. Finally, set the X-component of flow direction to 1 in Fluent, and use UDF to compile the data in the Y direction, as shown in Figure 4.20.

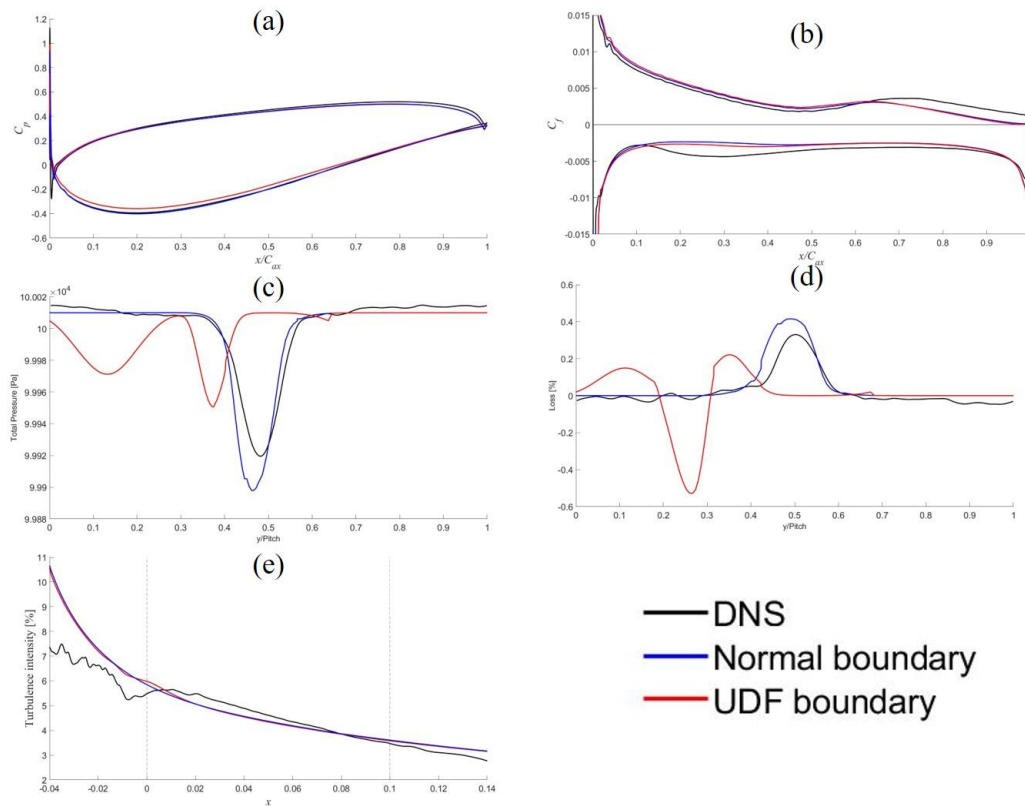


Fig 4.21: Comparison of parameters before and after UDF compilation boundary conditions

Figure 4.21 compares the changes of parameters before and after using UDF to compile import conditions. Among them, the pressure coefficient, skin friction coefficient and turbulence intensity did not change significantly before and after, but the total pressure distribution and loss changed significantly. The change of the wake region will change the distribution of the inlet and outlet pressures in a wide range.

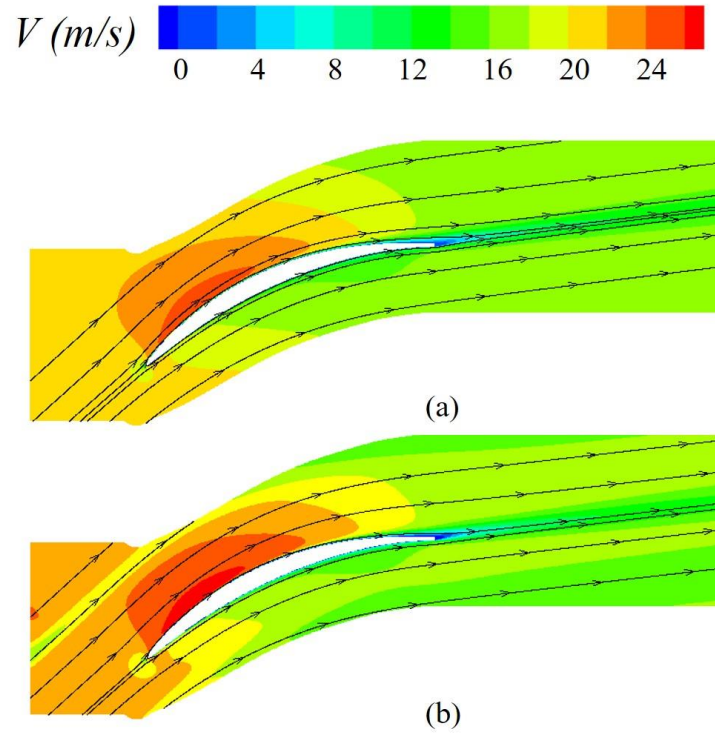


Fig 4.22: Velocity contours before and after UDF compilation of boundary conditions

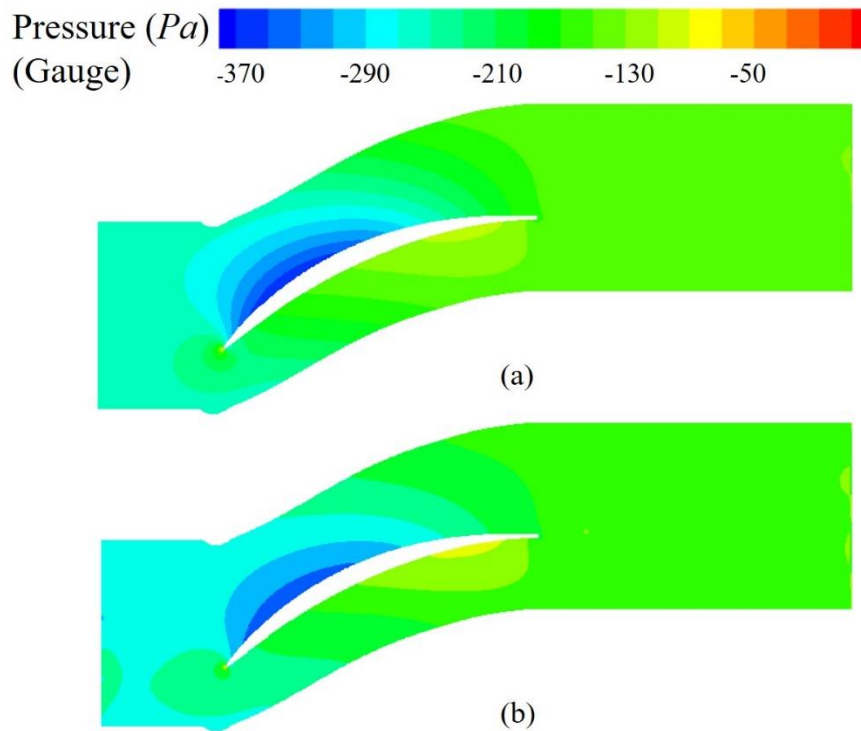


Fig 4.23: Pressure contours before and after UDF compilation of boundary conditions

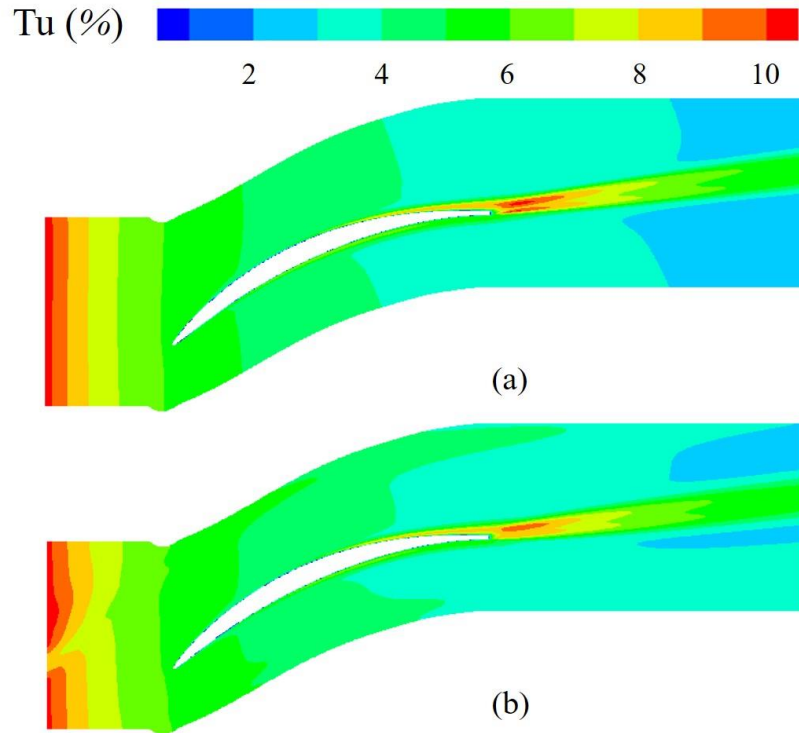


Fig 4.24: Turbulence intensity cloud map before and after UDF compilation of boundary conditions

Figure 4.22 compares the pressure contours, since the pressure at the inlet is not uniform, the distribution of the wake can be clearly observed at the inlet, which in turn affects the downstream flow field. Figure 4.23 compares the pressure contours, the distribution of static pressure is not disturbed by the distribution of the wake, which is very similar to the pressure distribution before UDF compilation. 4.24 compared the change of turbulence intensity. Due to the influence of the wake, the turbulence intensity in the wake region will be significantly lower than that of other locations, and the influence will gradually disappear when it is fully developed.

4.1.4 Conclusions

By comparing different turbulence models, it is found that for low-velocity compressor blades, the k-omega model with transition options has the closest results to DNS,

followed by the Transition SST model. But the two models did not show a particularly noticeable difference in the simulated results. When using RANS for numerical simulation, compared with DNS, it is necessary to increase the turbulence intensity at the inlet to a certain extent, instead of using the same inlet conditions as DNS, in order to obtain more accurate research results. In this paper, RANS uses a turbulence intensity equal to 10% compared to the case where the turbulence intensity is 6%, and RANS uses a turbulence intensity of 7% compared to the case with a turbulence intensity of 4%. The pressure coefficient obtained by RANS is basically the same as that of DNS, but there is a significant difference in skin friction coefficient, especially in the middle of the blade. For the distribution of turbulence intensity, due to the accuracy of the calculation, the turbulence intensity obtained by RANS shows a continuous downward trend, and the turbulence intensity decreases very rapidly at the inlet position, while DNS can accurately obtain the fluctuation of turbulence intensity. Under the condition that other conditions remain the same, only the turbulence intensity at the inlet is changed, the total pressure at the inlet and outlet is consistent with the DNS, the inlet static pressure is slightly larger than that of DNS, the outlet static pressure is slightly smaller than that of DNS, and the pressure loss is quite different from that of DNS. In the pressure and velocity contour, there is no significant difference in the distribution of pressure and velocity under each working condition, and changing the turbulence intensity at the inlet will not change the overall distribution.

When using UDF to define the inlet, the selection of the angle and position of the inlet will greatly affect the distribution of each parameter, especially the distribution of pressure. The difference is particularly evident in the velocity contour and the pressure contour. The non-uniform inlet conditions defined by the UDF are not suitable for simulating steady-state problems, and the distribution of positions has a very large impact on the results.

4.2 Unsteady case

4.2.1 URANS comparisons

In order to avoid the influence of the non-uniform boundary conditions defined by UDF on the flow field, and to better simulate the actual working conditions, this part will use URANS to simulate transient problems, capture different changes in each time, and make the simulation results more reliable.

First, using the above inlet pressure distribution to move along the Y-axis at a velocity of 16.1m/s, the inlet angle is kept at 42°, the turbulence intensity is 10%, and the parameters are compared 5 times in a period to find out the variation law and improve the simulation accuracy.

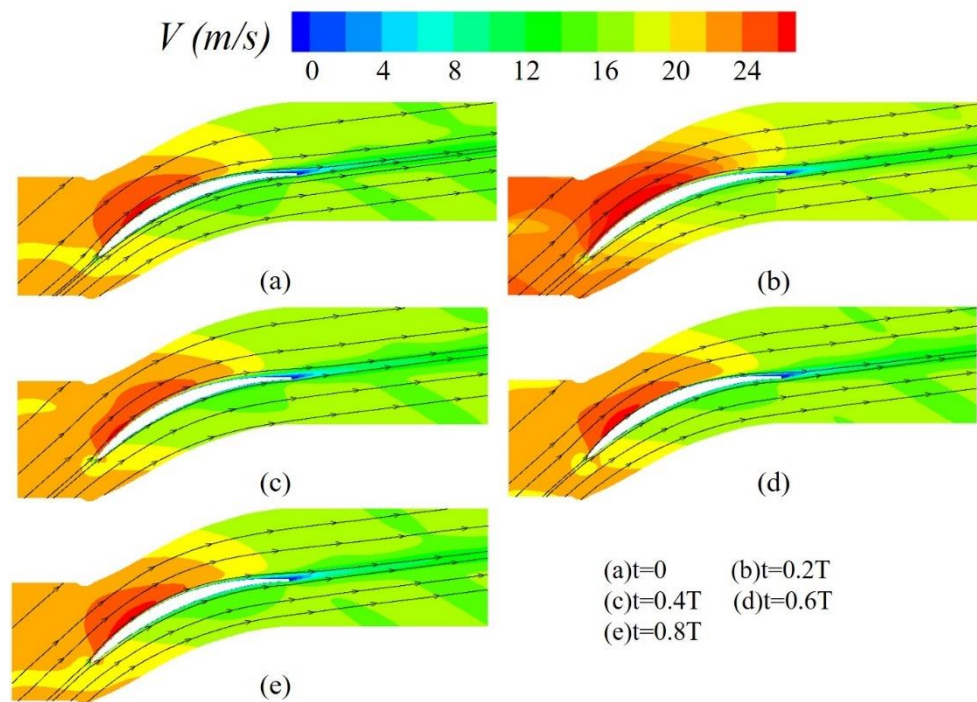


Fig 4.25: Velocity contour with UDF compiles inlet pressure

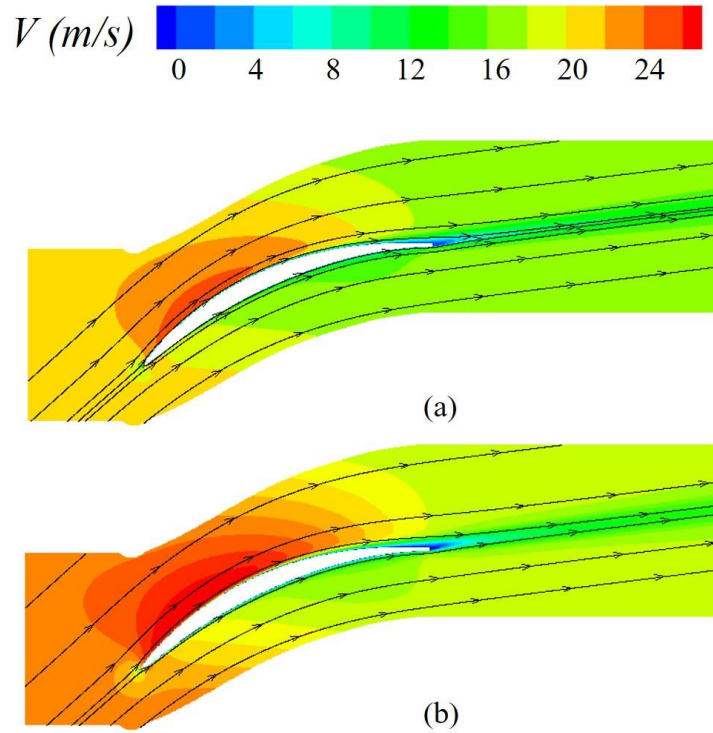


Fig 4.26: Comparison between RANS and average velocity contour with UDF compiles inlet pressure

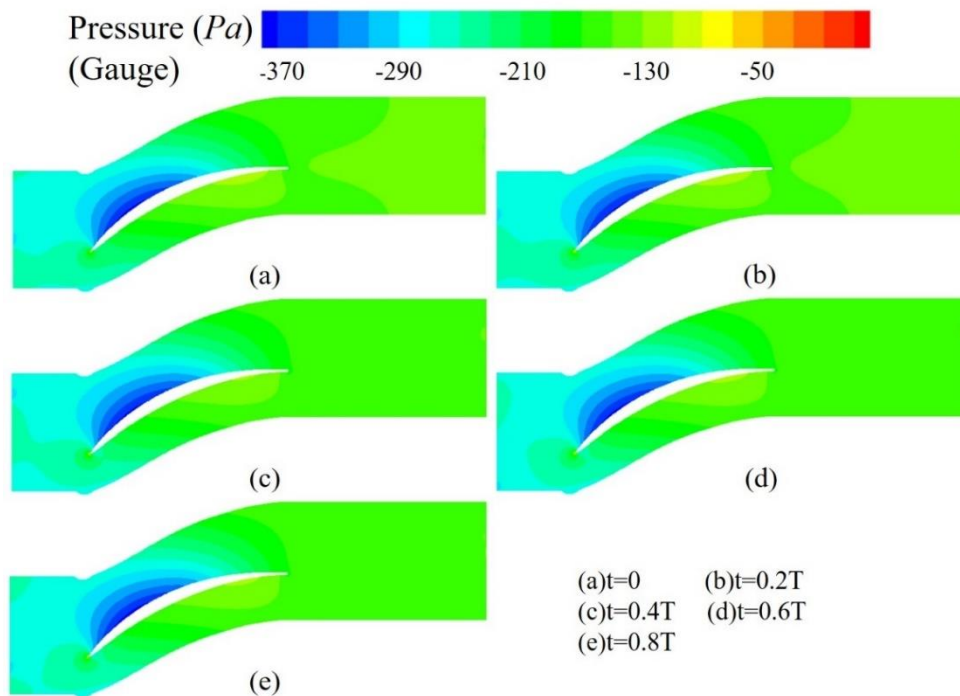


Fig 4.27: Pressure contour with UDF compiles inlet pressure

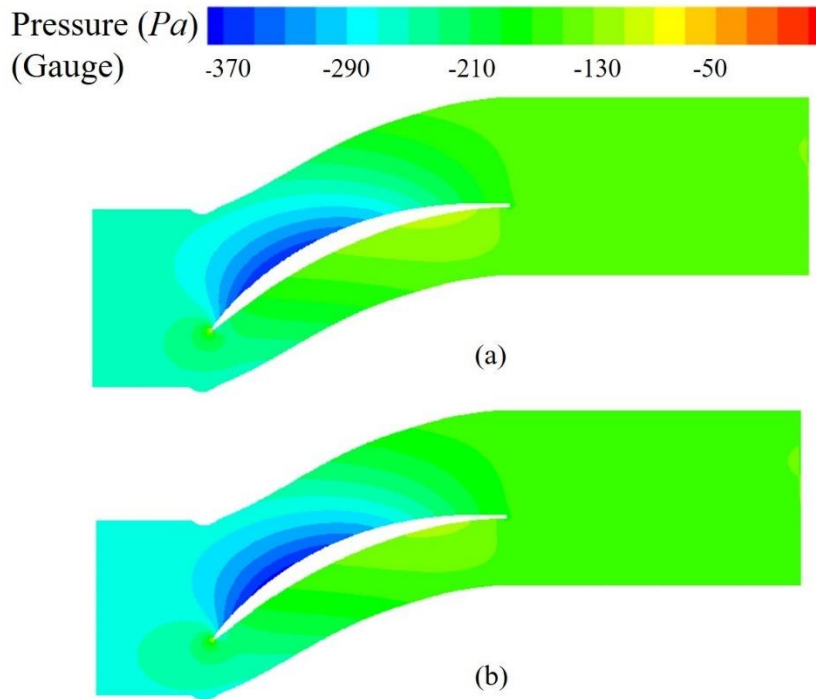


Fig 4.28: Comparison between RANS and average pressure contour with UDF compiles inlet pressure

As shown in Figure 4.25, in one period, due to the existence of the wake of the upper stage blade, there is an obvious low-velocity area at the inlet position, and the low-velocity area continues to develop upward at the same velocity. At the suction side of the blade, there is a local high-velocity area, and this area is constantly changing with the movement of the wake. When the wake is near the leading edge of the blade, the high-velocity area of the suction side expands in a large range. The overall velocity of the pressure side is lower than that of the suction side, and with the flow, the velocity decreases continuously throughout the flow channel. At the exit position, along the direction of the trailing edge, there is a low-velocity region, and the position remains relatively stable, at the same time, there is a strip-shaped low-velocity area at the exit position, which moves regularly towards the exit position. Figure 4.26 compares the velocity distribution obtained with RANS and the average velocity distribution obtained with URANS. It is not difficult to see that the velocity distribution is consistent on the whole, but the velocity obtained by URANS has a larger pressure gradient and

the absolute value of the velocity is slightly larger than that obtained by RANS, and the contrast is more obvious at the inlet position. In addition, the wake boundary obtained by URANS at the exit position is clearer, and there is also a large velocity gradient between the mainstream and the wake.

Figure 4.27 shows the distribution of static pressure at different times. At the inlet position, due to the influence of the previous stage wake, there is a very small area showing a smaller pressure. With the movement of the wake, the pressure at the inlet position increases with changes occur. When the flow passes through the blade, the static pressure distribution remains stable, and when it flows out of the blade, the position of the trailing edge of the blade changes periodically due to the different positions of the previous wake. Figure 4.28 compares the average pressure of RANS and URANS. The pressure distribution is very similar, and there is basically no difference in macro.

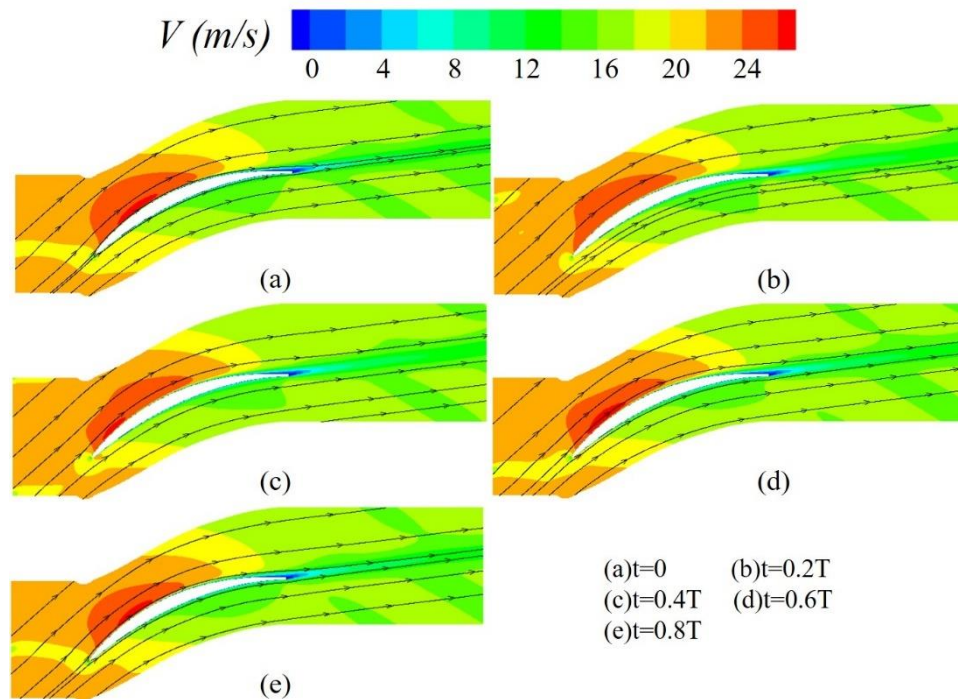


Fig 4.29: Velocity contour with UDF compiles inlet pressure and angle

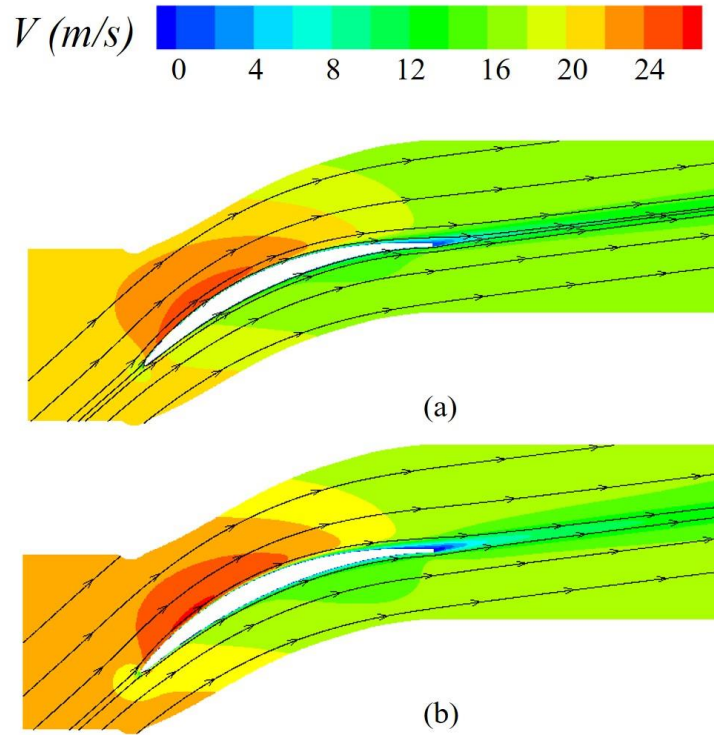


Fig 4.30: Comparison between RANS and average velocity contour with UDF compiles inlet pressure and angle

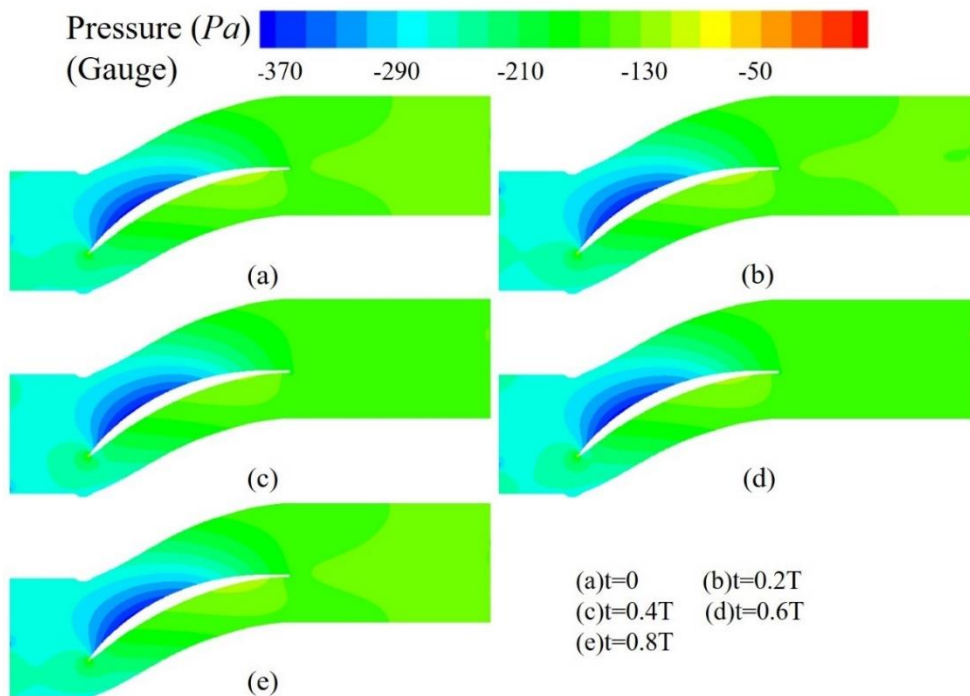


Fig 4.31: Pressure contour with UDF compiles inlet pressure and angle

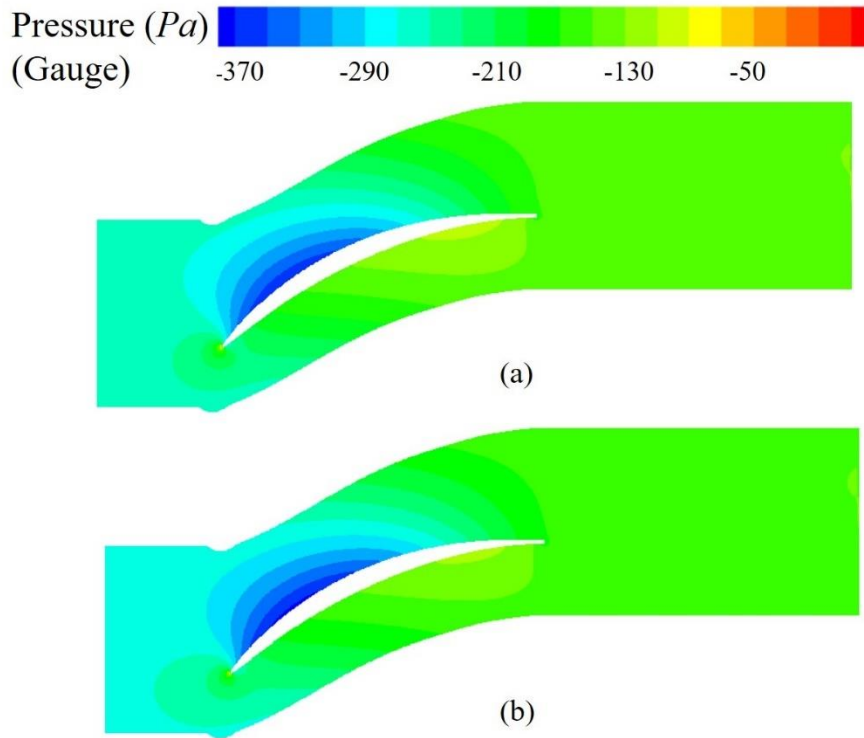


Fig 4.32: Comparison between RANS and average pressure contour with UDF compiles inlet pressure and angle

The boundary condition adds the intake angle, and also moves up along the Y-axis at a velocity of 16.1m/s, which is like the transient simulation of multi-stage cascades. Similarly, select 5 moments in each period for comparison and analyze their changing trends.

Figure 4.29 compares the velocity at different times. Compared with the previous example, it is found that the high-velocity area on the suction side is more stable, and there is no large-scale fluctuation. Other trends are basically similar to the previous example. Figure 4.30, Figure 4.31 and Figure 4.32 are basically same as the previous example.

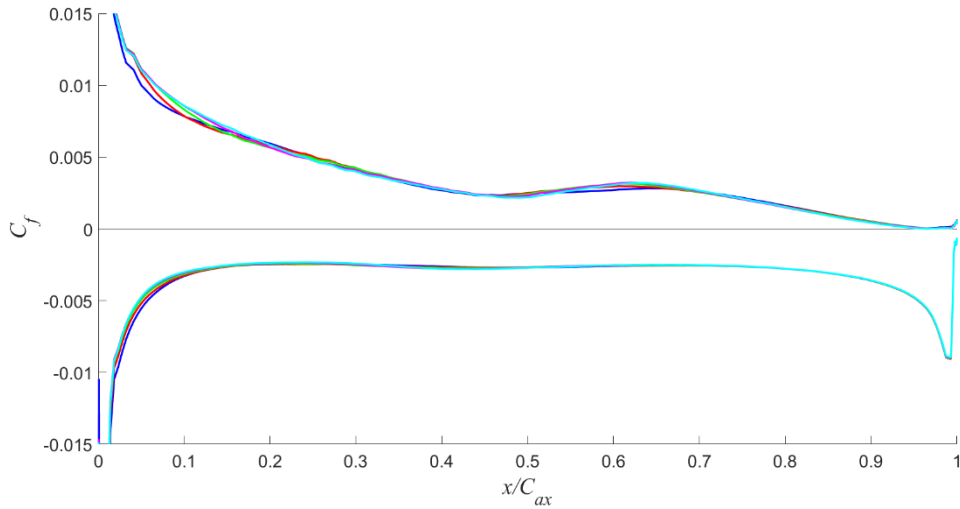


Fig 4.33: Skin friction coefficient with pressure inlet (URANS)

Figure 4.33 shows the variation of the blade skin friction coefficient over one period at the pressure inlet. The coefficient did not fluctuate significantly with the changing position of the wake.

In order to select more accurate inlet conditions, equivalent velocity inlets are used. The velocity is decomposed into the velocity in the X direction and the velocity in the Y direction. The velocity is obtained by extracting the velocity distribution at the pressure inlet, and after fitting, the velocity distribution shown below is obtained.

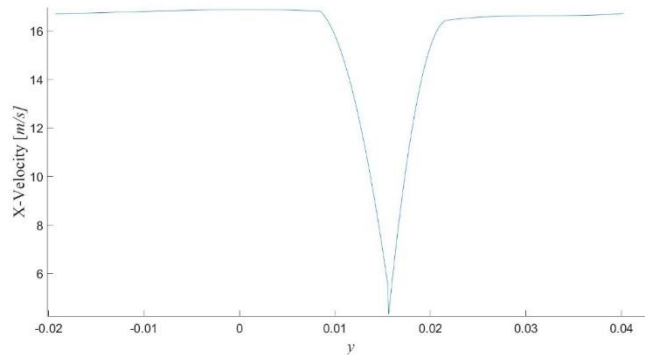


Fig 4.34: X-Velocity for Velocity Inlet

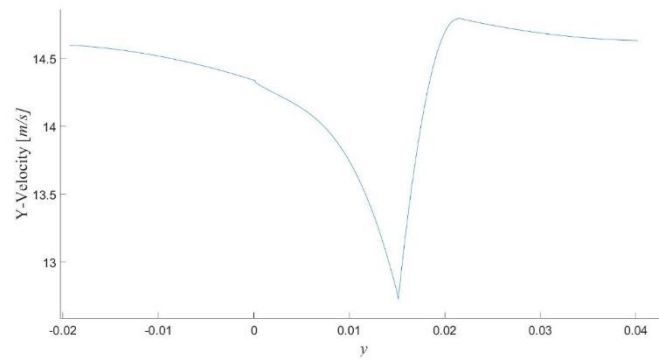


Fig 4.35: Y-Velocity for Velocity Inlet

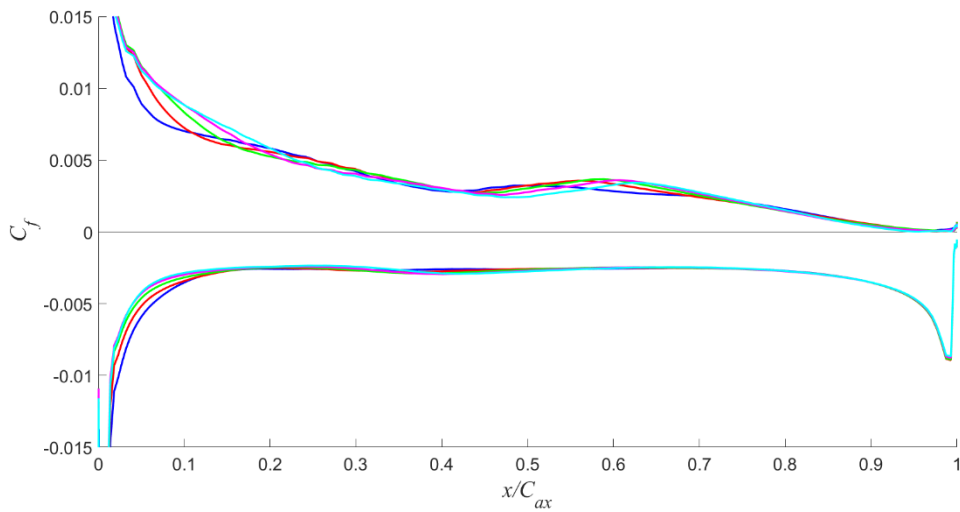


Fig 4.36: Skin friction coefficient with velocity inlet (URANS)

Plotting the skin friction coefficient at 5 times in a period, it is found that the fluctuation of the coefficient is slightly larger than that of the pressure inlet, the other trends are very similar.

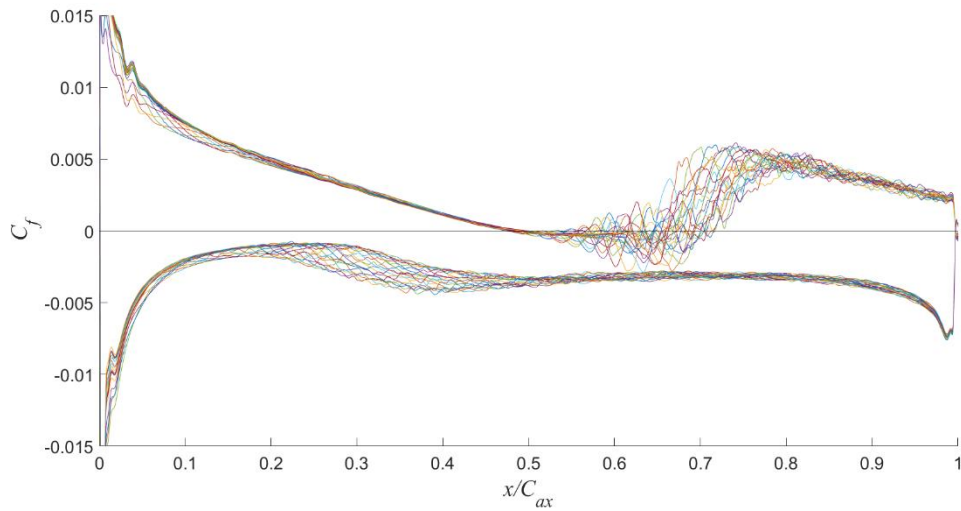


Fig 4.37: Skin friction coefficient for DNS

Figure 4.37 depicts the skin friction coefficient of DNS for 20 different phases in one cycle. It is very intuitive to find that the skin friction coefficient changes drastically at different time points, especially in the middle positions of the suction side and the middle front position of the pressure side. By comparison, it is found that the change of the skin friction coefficient of the velocity inlet is more same. In order to better capture the influence of small changes on the loss, the velocity inlet is selected as the inlet boundary of URANS.

In addition, the turbulence intensity of the DNS inlet is used in URANS to improve the fidelity of the numerical simulation, but due to the limitation of commercial software, UDF cannot be used to compile the turbulence intensity of the inlet, so the turbulence intensity is converted into Turbulent kinetic energy so that it has the same effect.

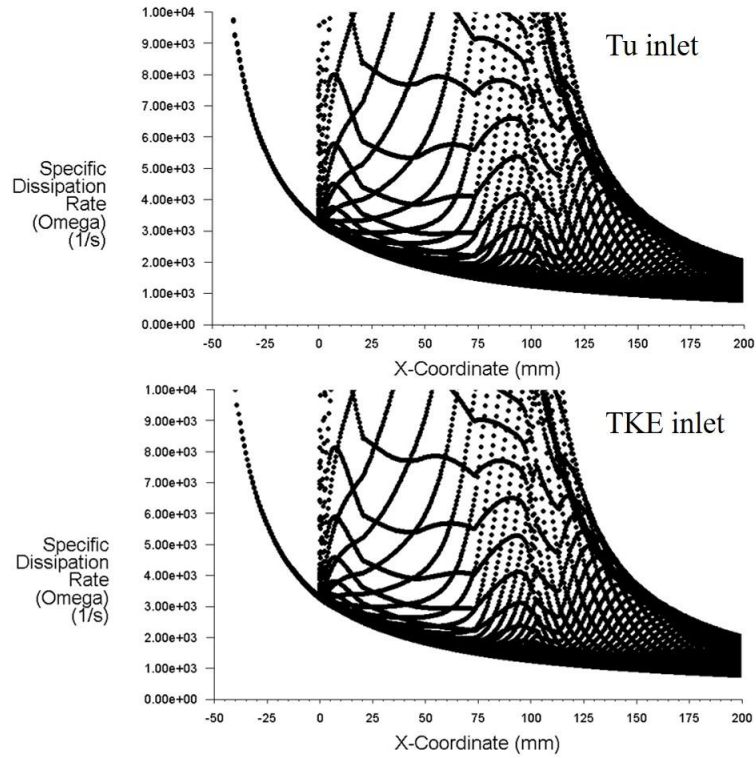


Fig 4.38: Comparison of specific dissipation rate using turbulence intensity inlet and turbulent kinetic energy inlet

By comparing the specific dissipation rate of the whole domain, it is found that the parameter distribution law and the numerical value are the same in the whole domain, so when the equivalent turbulent kinetic energy is used to define the inlet condition, it will not affect the results.

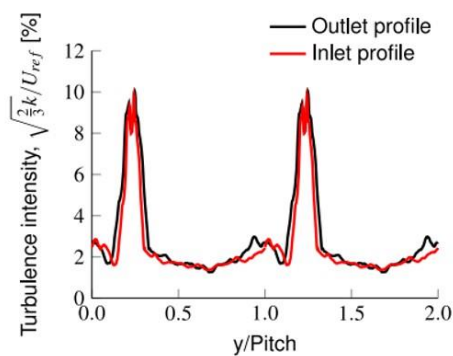


Fig 4.39: Average turbulence intensity at the inlet and at the sampling plane of the domain for the NACA65 testcase [27]

Figure 4.39 depicts the turbulence intensity at the inlet and outlet of the DNS. In the wake region, the turbulence intensity reaches a maximum value of 10%, while in other regions, the turbulence intensity remains roughly constant at about 3%. Compiled by UDF, the turbulent flow intensity is equivalent to turbulent kinetic energy, which acts on the inlet of URANS, and the fidelity of numerical simulation is improved by comparing the changes of the skin friction coefficient in one cycle.

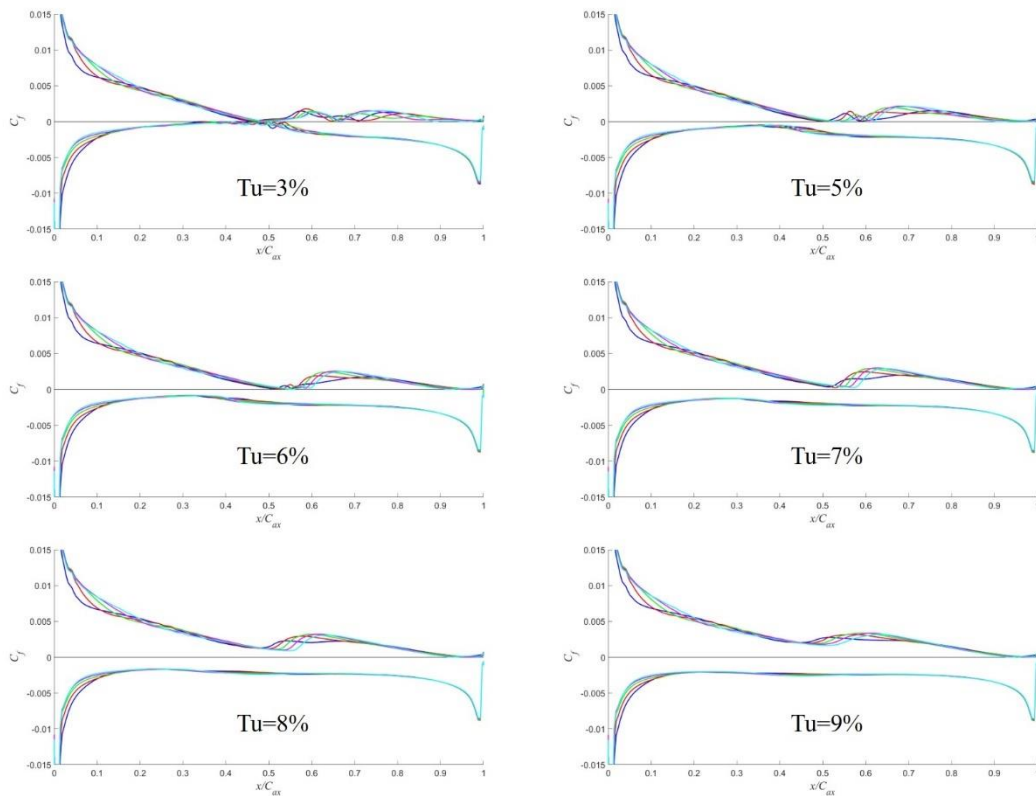


Fig 4.40: Skin friction coefficient comparison (Turbulence intensity is 10% in wake region)

First, keep the turbulence intensity in the wake region at 10% in Figure 4.40, and change the turbulence intensity in other regions from 3% to 9%. When the turbulence intensity is small, the skin friction coefficient on the suction side changes greatly. With the increasement of the turbulence intensity, the fluctuation of the skin friction coefficient becomes small and tends to be stable. Especially when the turbulence intensity reaches 9%, the change of the skin friction coefficient of the suction side is the smallest.

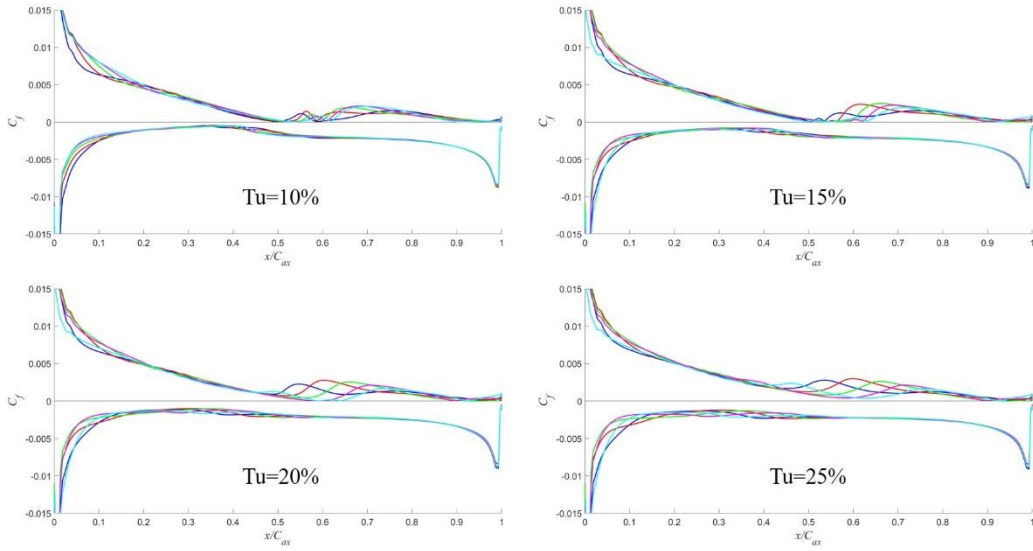


Fig 4.41: Skin friction coefficient comparison (Turbulence intensity is 5% except in wake region)

Secondly, the turbulence intensity in the wake region was changed, while the turbulence intensity in other regions was kept at 5%. With the increasement of turbulence intensity in the wake region, the variation trend of the skin friction coefficient on the suction side is more obvious, and on the pressure side, with the increasement of turbulence intensity, the skin friction coefficient changes slightly, but it is not obvious enough.

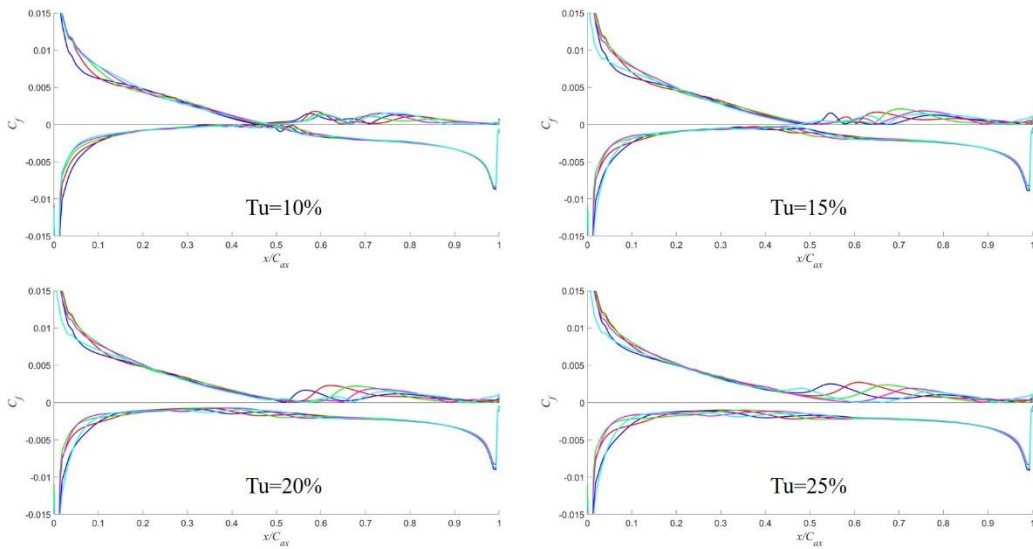


Fig 4.42: Skin friction coefficient comparison (Turbulence intensity is 3% except in wake region)

The third time is also to change the turbulence intensity in the wake area, but the turbulence intensity in other areas is kept at 3%. The change trend is basically same as that of the previous example, but due to the small turbulence intensity, the variation range of the skin friction coefficient is not as large as that of the previous example.

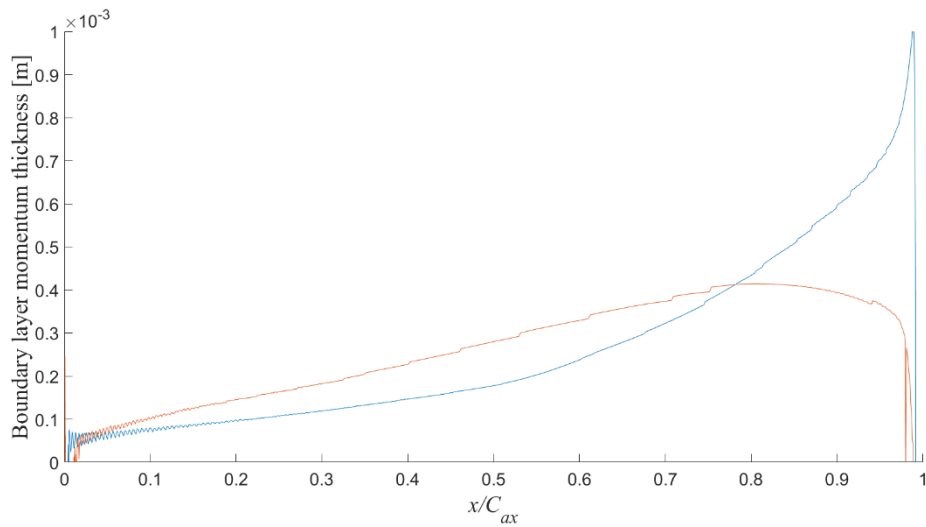


Fig 4.43: Boundary layer momentum thickness (URANS)

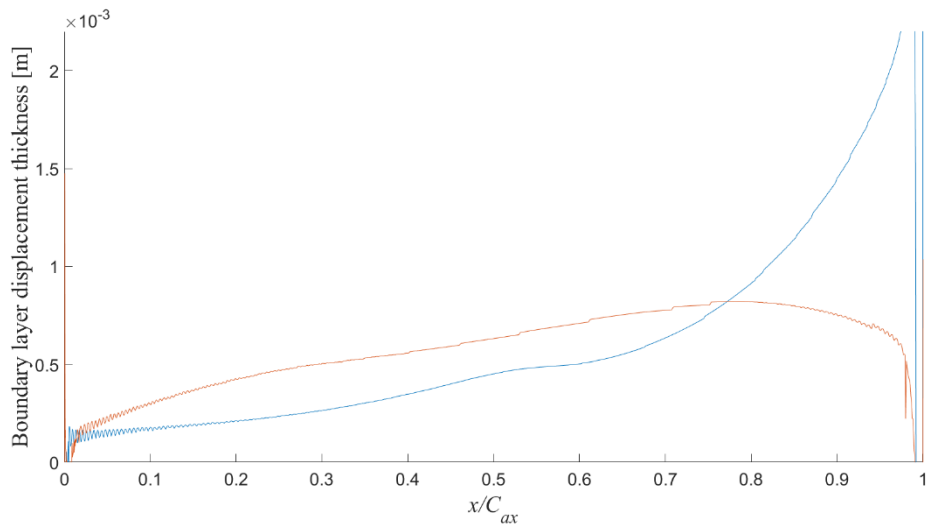


Fig 4.44: Boundary layer displacement thickness (URANS)

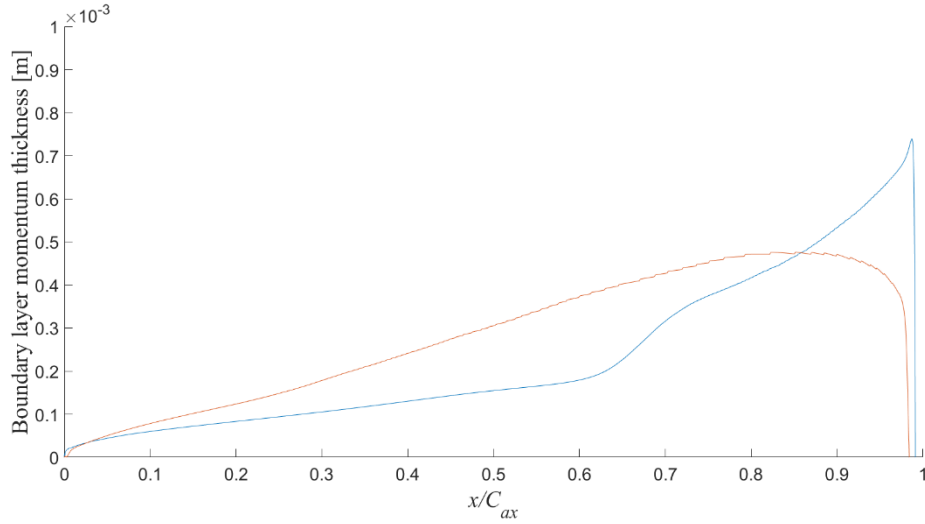


Fig 4.45: Boundary layer momentum thickness (DNS)

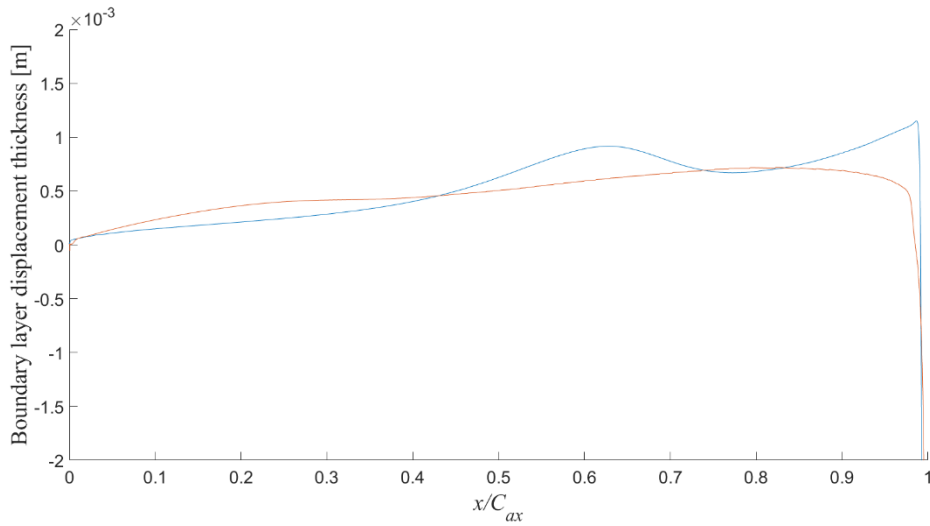


Fig 4.46: Boundary layer displacement thickness (DNS)

$$C_{pb} = (P_b - P_{ref}) / (0.5\rho V_{ref}^2) \quad (4.2)$$

$$\xi = \frac{\Delta P_0}{0.5\rho V_{te}^2} = -\frac{C_{pb}t}{w} + \frac{2\theta}{w} + \left(\frac{\delta^* + t_e}{w}\right)^2 \quad (4.3)$$

δ^*	Boundary layer displacement thickness	2.01	mm
C_{pb}	Base pressure coefficient	0.34	
t_e	Trailing edge thickness	1.23	mm

w	Throat width	55	mm
θ	Boundary layer momentum thickness	0.63	mm
ρ	Fluid density	1.1721994	kg/m ³
V_{te}	Flow velocity just before the trailing edge	16.191002	m/s
P_1^*	Inlet stagnation pressure	99998.86	Pa
P_2^*	Outlet stagnation pressure	99996.58	Pa
ξ	Pressure loss	1.88	%

Table 4.5: Pressure loss for URANS

δ^*	Boundary layer displacement thickness	1.01	mm
C_{pb}	Base pressure coefficient	0.35	
t_e	Trailing edge thickness	1.23	mm
w	Throat width	55	mm
θ	Boundary layer momentum thickness	0.62	mm
ξ	Pressure loss	1.64	%

Table 4.6: Pressure loss for DNS

The definition of stagnation pressure loss is shown in Equation 4.3. It is worth noting that adopting this method has nothing to do with the mixing process, because the mixing process is unstable, the formation of the Karman vortex street and the viscous loss caused by the vortex account for the majority of the losses. It is difficult to predict the details of the process, and the overall outcome can be predicted using this method.

Use Matlab to draw the distribution curve of boundary layer displacement thickness and boundary layer momentum thickness, take the extracted value at 95% of the C_{ax} position, and calculate the pressure loss values of URANS and DNS. After comparison, it is found that after using URANS, the pressure loss is significantly smaller than that obtained when using RANS, and the final result is about 1.88%, which is very close to the pressure loss of DNS 1.64%.

4.2.2 Conclusions

When URANS uses the pressure inlet and the velocity inlet, the pressure distribution, velocity distribution and turbulence intensity distribution in the entire domain are very similar, but in the comparison of the skin friction coefficient, the calculation example using the velocity inlet can get closer to DNS. Therefore, when using URANS for numerical simulation of low-velocity cascades, compared with the pressure inlet, the velocity inlet can obtain results that are closer to DNS.

In order to make the results of URANS more accurate, it is necessary to change the turbulence intensity of the inlet. When the turbulence intensity of the wake region or the turbulence intensity of other regions increases, the variation range of the skin friction coefficient can be larger to a certain extent.

However, when using URANS to calculate the pressure loss, compared with RANS, the result is closer to the pressure loss of DNS. The final pressure loss of URANS is 1.88%, which is very close to the pressure loss of 1.64% of DNS.

4.3 Conclusions

When RANS is used to numerically simulate the low-velocity compressor cascade, and the parameters are comprehensively compared, the k-omega model with transition options is the most accurate turbulence model, followed by the Transition SST model. For the pressure coefficient, the results of RANS are very similar to the results of DNS, but the skin friction coefficient obtained by RANS is still quite different from that of DNS. In order to make the results more accurate, it is necessary to appropriately increase the turbulence intensity at the inlet of RANS by about 4%. The total pressure at the inlet and outlet of RANS is the same as that of DNS. The inlet static pressure is slightly larger than that of DNS, and the outlet static pressure is slightly lower than that of DNS, but the pressure loss is much larger. When using UDF to compile the boundary

conditions, although it can be like the actual situation, due to the existence of the wake, it will have a significant impact on the results.

For URANS, the pressure inlet and velocity inlet have small influence on the distribution of pressure and velocity, but when the velocity inlet is adopted, the change of the skin friction coefficient is more obvious, which is more same with the results of DNS. Increasing the turbulence intensity at the inlet can make the skin friction coefficient change more violently, which can make the result closer to DNS, but there is still a big difference on the whole. Importantly, the pressure loss calculated with URANS is closer to that of DNS, making the calculated results more accurate.

5 Conclusions and Recommendations for Future Work

The first chapter introduces the research background. Since the concept of low-carbon environmental protection is deeply rooted in the hearts of the people and the requirements for improving engine efficiency, the fidelity of numerical simulation needs to be further improved. Since DNS and LES require high-performance computers, this paper uses RANS and URANS. Numerical simulation of low-velocity cascade is carried out, and the boundary conditions are changed in various ways to improve the accuracy of numerical simulation.

The second chapter introduces the research status of related fields, including research on turbulence models and turbomachinery. Numerical simulation has become an indispensable research method in scientific research, and has played a vital role in accelerating the progress of the project and saving the cost of experiments. Due to the continuous improvement of computer performance, numerical simulation is also experiencing rapid development, but how to improve the accuracy of numerical simulation is one of the hotspots of research in various fields.

The third chapter introduces the commonly used turbulence models for numerical simulation, drawing meshes, verifying mesh independence and model comparison. For the numerical simulation of low-velocity cascades, the requirements for the number of grids are relatively low, and the number of grids of 50,000 can already ensure the accuracy of the numerical simulation. For turbulence models k-omega model with transition options is the most accurate turbulence model, followed by the Transition SST model.

The fourth chapter compares the differences between RANS/URANS and DNS, and improves the accuracy of numerical simulation in various ways. For steady-state problems, an appropriate increase in the turbulence intensity at the inlet can make the results closer to DNS, and the skin friction coefficient and pressure loss are still quite different from DNS, and further optimization is needed. When compiling the inlet boundary conditions with the UDF, the wake region has a very significant effect on the results. For transient problems, velocity inlets are more suitable as boundary conditions for URANS. Increasing the turbulence intensity of the inlet can make the skin friction coefficient have more obvious fluctuations, but the difference with DNS is still very large. Luckily, the pressure loss calculated with URANS is closer to that of DNS, making the calculated results more accurate.

For future research work, it can focus on the study of URANS, such as compiling the turbulence intensity through UDF to find a better solution. At the same time, the FLUENT parameter can be modified, and the changes of the parameter before and after the modification can be compared, so that the result of URANS is closer to the DNS.

Acknowledge

The academic career of the Politecnico di Torino will come to an end with the conclusion of this dissertation. Even if you are reluctant to give up, you must continue to move forward.

First of all, I would like to thank China and Italy, two great countries, for giving me a good learning platform. Thanks to Harbin, a beautiful city in China, and thanks to Turin and Genoa, two attractive cities in Italy. I will remember the snowy mountains and cars in Turin, I will remember the waves and beaches in Genoa. I will even remember the smiles from the heart of the Italian people. The meticulous care made me feel warm in a foreign country.

Thanks to Prof. Roberto Marsilio of the Politecnico di Torino for his guidance on my graduation thesis. The professor always responds to emails very promptly and quickly, which makes me feel warm. I would like to thank Prof. Pietro Zunino, Prof. Davide Lengani and Prof. Dario Barsi of the University of Genoa for giving me a chance to come to Genoa, and for their guidance throughout my thesis. Thanks to Dr. Pawel Przytarski, University of Cambridge, the research of this dissertation builds on the research that Dr. Pawel Przytarski did during his time at the University of Cambridge. It is because of Dr. Pawel Przytarski's detailed guidance that I can complete this dissertation. Thanks to Dr. Yang, a CFD expert at the University of Genoa, who always helps me solve problems in time when I encounter problems. I would like to thank Professor Wang Zhongyi and Professor Qu Yonglei from Harbin Engineering University for their meticulous care for me and I was able to complete my master's study in Italy.

Thanks to my university classmates, high school classmates and junior high school classmates, thanks to Li Yuanlin for explaining economics to me, thanks to Dr. Zhang

Wenchen of Shanghai Jiaotong University for explaining material science to me, and thanks to my good friend Lu Shuai who always listened to my past experiences and helped me during the Chinese New Year Visiting my parents, thanking my good friends for helping me visit my sick mother, thanking Shan Jiahao for helping me in time when I was poor, and thanking my college classmates for helping me with my studies.

Thanks to every friend in Turin, Wang Shixian, Chen Hang, Chen Ze, Guo Xiaoshuang, Wang Renju, Meng Shisen, etc. for their help and care to me. I would like to thank my roommates Chen Boyu and Zhao Zheng in Genoa for their tolerance and help.

Thanks to Dr Xie Jin from UNSW, we published the first paper of my academic career together.

I would like to thank my brother Li in Turin for taking me in during my exams. I also thank my lawyer sister for answering various questions for me.

Finally, I would like to thank myself and the self who never gave up after experiencing countless difficulties.

Heaven will assign great responsibilities to the people of this country, and they must first work hard on their hearts and minds.

Bibliography

- [1] Denton J D. Loss mechanisms in turbomachines[M]. American Society of Mechanical Engineers, 1993.
- [2] Tucker P G. Trends in turbomachinery turbulence treatments[J]. Progress in Aerospace Sciences, 2013, 63: 1-32.
- [3] Denton J D. Some limitations of turbomachinery CFD[C]//Turbo Expo: Power for Land, Sea, and Air. 2010, 44021: 735-745.
- [4] Menter F R, Langtry R, Hansen T. CFD simulation of turbomachinery flows-verification, validation and modeling[C]//European Congress on Computational Methods in Applied Sciences and Engineering, Jyvsykl. 2004, 1: 1-14.
- [5] Krein A, Williams G. Flightpath 2050: Europe's vision for aeronautics[J]. Innovation for Sustainable Aviation in a Global Environment: Proceedings of the Sixth European Aeronautics Days, Madrid, 2012, 30.
- [6] Tyacke J, Vadlamani N R, Trojak W, et al. Turbomachinery simulation challenges and the future[J]. Progress in Aerospace Sciences, 2019, 110: 100554.
- [7] Moin P, Mahesh K. Direct numerical simulation: a tool in turbulence research[J]. Annual review of fluid mechanics, 1998, 30(1): 539-578.
- [8] Kaneda Y, Ishihara T. High-resolution direct numerical simulation of turbulence[J]. Journal of Turbulence, 2006 (7): N20.
- [9] Coleman G N, Sandberg R D. A primer on direct numerical simulation of turbulence-methods, procedures and guidelines[J]. 2010.
- [10] Piomelli U. Large-eddy simulation: achievements and challenges[J]. Progress in aerospace sciences, 1999, 35(4): 335-362.
- [11] Mason P J. Large-eddy simulation: A critical review of the technique[J]. Quarterly Journal of the Royal Meteorological Society, 1994, 120(515): 1-26.
- [12] Boris J P, Grinstein F F, Oran E S, et al. New insights into large eddy simulation[J]. Fluid dynamics research, 1992, 10(4-6): 199.

- [13] Alfonsi G. Reynolds-averaged Navier–Stokes equations for turbulence modeling[J]. *Applied Mechanics Reviews*, 2009, 62(4).
- [14] Chen H C, Patel V C, Ju S. Solutions of Reynolds-averaged Navier-Stokes equations for three-dimensional incompressible flows[J]. *Journal of Computational Physics*, 1990, 88(2): 305-336.
- [15] Wilcox D C. *Turbulence modeling for CFD*[M]. La Canada, CA: DCW industries, 1998.
- [16] Slotnick J P, Khodadoust A, Alonso J, et al. *CFD vision 2030 study: a path to revolutionary computational aerosciences*[R]. 2014.
- [17] Denton JD, Dawes WN. *Computational fluid dynamics for turbomachinery design*. *Proceedings of the Institution of Mechanical Engineers, Part C: Journal of Mechanical Engineering Science*. 1998;213(2):107-124.
- [18] Vassberg J, Dehaan M, Rivers M, et al. *Development of a common research model for applied CFD validation studies*[C]//26th AIAA applied aerodynamics conference. 2008: 6919.
- [19] Fujii K. *Progress and future prospects of CFD in aerospace—Wind tunnel and beyond*[J]. *Progress in Aerospace Sciences*, 2005, 41(6): 455-470.
- [20] Lynch F T. *Commercial transports- Aerodynamic design for cruise performance efficiency*[J]. *Transonic aerodynamics*, 1981: 81-147.
- [21] Chapman D. *Opening remarks*. In: *Proceedings of the workshop on future computer requirements for computational aerodynamics*, NASA CP 2032; 1978.
- [22] Yang Y, Ma H. *Hybrid RANS/LES study of tip leakage vortex instability and turbulence characteristics of a transonic turbine cascade*[J]. *Aerospace Science and Technology*, 2022, 128: 107758.
- [23] Tiberghien M, Hennink A, Kloosterman J L, et al. *A high-order discontinuous Galerkin solver for the incompressible RANS equations coupled to the $k-\epsilon$ turbulence model*[J]. *Computers & Fluids*, 2020, 212: 104710.

- [24] Kubacki S, Borzecki T, Dick E. Prediction of bypass and separation-induced transition with an algebraic intermittency model[J]. ERCOFTAC BULLETIN, 2016, 108: 48-53.
- [25] Walters D K. Physical interpretation of transition-sensitive RANS models employing the laminar kinetic energy concept[J]. Ercoftac Bulletin, 2009, 80: 67-71.
- [26] Przytarski P J, Wheeler A P S. The Effect of Gapping on Compressor Performance[J]. Journal of Turbomachinery, 2020, 142(12).
- [27] Przytarski P J, Wheeler A P S. Accurate prediction of loss using high fidelity methods[C]. Turbo Expo: Power for Land, Sea, and Air. American Society of Mechanical Engineers, 2018, 51012: V02CT42A051.
- [28] Zaki T A, Wissink J G, Durbin P A, et al. Direct computations of boundary layers distorted by migrating wakes in a linear compressor cascade[J]. Flow, turbulence and combustion, 2009, 83(3): 307-322.
- [29] Hilgenfeld L, Pfitzner M. Unsteady boundary layer development due to wake passing effects on a highly loaded linear compressor cascade[J]. J. Turbomach., 2004, 126(4): 493-500.
- [30] Bell R, Fottner L. Investigations of shock/boundary-layer interaction in a highly loaded compressor cascade[C]//Turbo Expo: Power for Land, Sea, and Air. American Society of Mechanical Engineers, 1995, 78781: V001T01A016.
- [31] ANSYS Fluent Theory Guide.
- [32] Spalart P R. Strategies for turbulence modelling and simulations[J]. International journal of heat and fluid flow, 2000, 21(3): 252-263.
- [33] Gopalan H, Heinz S, Stöllinger M K. A unified RANS–LES model: Computational development, accuracy and cost[J]. Journal of Computational Physics, 2013, 249: 249-274.
- [34] Hanjalic K. Will RANS survive LES? A view of perspectives[J]. 2005.
- [35] Spalart P R. Strategies for turbulence modelling and simulations[J]. International journal of heat and fluid flow, 2000, 21(3): 252-263.

- [36] Gavrilakis S. Numerical simulation of low-Reynolds-number turbulent flow through a straight square duct[J]. *Journal of Fluid Mechanics*, 1992, 244: 101-129.
- [37] Lodaes D, Manzanero J, Ferrer E, et al. An entropy–stable discontinuous Galerkin approximation of the Spalart–Allmaras turbulence model for the compressible Reynolds Averaged Navier–Stokes equations[J]. *Journal of Computational Physics*, 2022, 455: 110998.
- [38] Bouchard M, Marty J, Deck S, et al. Validation of correlations-based transition modeling strategies applied to the Spalart-Allmaras turbulence model for the computation of separation-induced transition[J]. *Aerospace Science and Technology*, 2021, 119: 107045.
- [39] Li W, Liu Y. Numerical investigation of corner separation flow using Spalart-Allmaras model with various modifications[J]. *Aerospace Science and Technology*, 2022: 107682.
- [40] Rocha P A C, Rocha H H B, Carneiro F O M, et al. k – ω SST (shear stress transport) turbulence model calibration: A case study on a small scale horizontal axis wind turbine[J]. *Energy*, 2014, 65: 412-418.
- [41] Rocha P A C, Rocha H H B, Carneiro F O M, et al. A case study on the calibration of the k – ω SST (shear stress transport) turbulence model for small scale wind turbines designed with cambered and symmetrical airfoils[J]. *Energy*, 2016, 97: 144-150.
- [42] Rahman M M. Capturing transition and non-transition flows with a new shear stress transport model[J]. *Chinese Journal of Aeronautics*, 2022.
- [43] Raje P, Sinha K. Anisotropic SST turbulence model for shock-boundary layer interaction[J]. *Computers & Fluids*, 2021, 228: 105072.
- [44] Li J, Zhong C, Pan D, et al. A gas-kinetic scheme coupled with SST model for turbulent flows[J]. *Computers & Mathematics with Applications*, 2019, 78(4): 1227-1242.
- [45] Jones W P, Launder B E. The calculation of low-Reynolds-number phenomena with a two-equation model of turbulence[J]. *International Journal of Heat and Mass Transfer*, 1973, 16(6): 1119-1130.

- [46] Salimipour E. A modification of the k - k_L - ω turbulence model for simulation of short and long separation bubbles[J]. *Computers & Fluids*, 2019, 181: 67-76.
- [47] Shome B. Numerical study of oscillating boundary layer flow over a flat plate using k - k_L - ω turbulence model[J]. *International journal of heat and fluid flow*, 2013, 42: 131-138.
- [48] Lorini M, Bassi F, Colombo A, et al. Discontinuous Galerkin solution of the RANS and k_L - k - $\log(\omega)$ equations for natural and bypass transition[J]. *Computers & Fluids*, 2021, 214: 104767.